Androgen loss accelerates brain tumour growth via HPA axis activation

https://doi.org/10.1038/s41586-026-10451-5
Received: 4 March 2024
Accepted: 25 March 2026

Juyeun Lee[1], Yoon-Mi Chung[2,3,21], Daniel J. Silver[1,4,5,6,21], Yue Hao[7,21], Dylan Scott Lykke Harwood[8,9], Alyssa Ealy[10], Amanda M. Serapiglia[10], Lee Curtin[11,12], Julia R. Benedetti[13], Christine Ann Pittman Ballard[13], Kamya Lapsley[10], Andrea Alvarez-Vazquez[1], Jessica Goldberg[1], Cathy Li[1], Sehaj Kaur[1], Rian Neal[1], Sabrina Z. Wang[1,14], Kristen E. Kay[1,15], Josephine Volovetz[1,15], Ellen S. Hong[1,14], R'ay Fodor[1], Jakub Jarmula[1], Michael Nicosia[16], Joshua B. Rubin[17,18], Kristin R. Swanson[11,12], Quinn T. Ostrom[13,19,20], Nikhil Panicker[10], Bjarne Winther Kristensen[8,9], Michael Berens[7], Nima Sharifi[2,3] & Justin D. Lathia[1,4,5,6,9] ✉

Many cancers, including glioblastoma (GBM), show a male-biased incidence and associated worse outcomes[1]. The mechanisms that underlie this sex difference remain unclear but may involve an immune response[2] that is partly driven by sex hormones such as androgens. Such hormones are thought to suppress antitumour T cell immunity and to promote tumour progression[3,4]. However, here we report a previously unreported tumour-suppressive role for androgens in brain tumours. Using mouse models, we demonstrate that androgen loss via castration accelerates intracranial tumour growth, whereas the opposite effect (delayed tumour growth) is observed in extracranial tumours. Similar effects were observed in male patients with GBM, in whom testosterone treatment significantly reduced the risk of death. In male mice with GBM tumours, castration-induced systemic T cell dysfunction driven by increased levels of serum glucocorticoids, which act on myeloid cells to promote an immunosuppressive tumour microenvironment. Mechanistically, hyperactivation of the hypothalamus–pituitary–adrenal axis in castrated mice with GBM is driven by increased neuroinflammatory signalling through IL-1β and TNF. Spatial transcriptomic analysis further revealed that androgen loss enhances inflammasome activation in microglia, which promotes this neuroinflammatory state. Together, our findings demonstrate that brain tumours drive distinct neuroinflammatory and neuroendocrine pathways in the androgen-deprived setting and highlight organ-specific regulation of antitumour immunity.

Sex differences in cancer have long been recognized in non-reproductive organs, such as bladder, colorectal system, lung, skin and brain[1,5,6]. Indeed, recent efforts have started to highlight the mechanisms that underlie these differences. In general, male individuals exhibit a higher incidence and poorer outcomes than female individuals across these cancers. Sex hormones and sex chromosomes, including the loss of the Y chromosome[7,8], are the main factors that drive tumour-intrinsic[9] or tumour-extrinsic[10] sex differences in cancers. Recently, a crucial role for androgens in antitumour immunity and their impact on immune checkpoint inhibitor treatment have been identified. Specifically, inhibition of androgen receptor (AR) signalling enhances the efficacy of anti-PD1 treatment in mouse models of castration-resistant prostate cancer[11], bladder cancer[4] and colon cancer[3], which was due to increased T cell exhaustion induced by AR signalling[3,4]. Therefore, blocking AR can synergize with anti-PD1 and PD-L1 blockade to reinvigorate T cell function.

GBM is the most common and malignant primary brain tumour. GBM also displays sex differences, with poorer outcomes observed in

---

[1]Department of Cancer Sciences, Cleveland Clinic Research, Cleveland, OH, USA. [2]Desai Sethi Urology Institute, University of Miami Miller School of Medicine, Miami, FL, USA. [3]Sylvester Comprehensive Cancer Center, University of Miami Miller School of Medicine, Miami, FL, USA. [4]Rose Ella Burkhardt Brain Tumor Center, Cleveland Clinic, Cleveland, OH, USA. [5]Case Comprehensive Cancer Center, Cleveland, OH, USA. [6]Department of Pathology, Cleveland Clinic Lerner College of Medicine, Case Western Reserve University, Cleveland, OH, USA. [7]TGen, Translational Genomics Research Institute, Phoenix, AZ, USA. [8]The Bartholin Institute, Department of Pathology, Rigshospitalet, Copenhagen University Hospital, Copenhagen, Denmark. [9]Department of Clinical Medicine and Biotech Research and Innovation Centre (BRIC), University of Copenhagen, Copenhagen, Denmark. [10]Department of Neurosciences, Cleveland Clinic Research, Cleveland, OH, USA. [11]MOSAIC (Mathematical Oncology Systems Analysis of Imaging Center), Cedars-Sinai, Los Angeles, CA, USA. [12]Department of Neurosurgery, Computational Biomedicine, and Pathology & Laboratory Medicine, Cedars-Sinai, Los Angeles, CA, USA. [13]Department of Neurosurgery, Duke University School of Medicine, Durham, NC, USA. [14]Medical Scientist Training Program, Department of Medicine, Case Western Reserve University, Cleveland, OH, USA. [15]Department of Molecular Medicine, Cleveland Clinic Lerner College of Medicine, Case Western Reserve University, Cleveland, OH, USA. [16]Department of Inflammation and Immunity, Cleveland Clinic Research, Cleveland, OH, USA. [17]Department of Pediatrics, St Louis Children's Hospital, Washington University School of Medicine, St Louis, MO, USA. [18]Department of Neuroscience, Washington University School of Medicine, St Louis, MO, USA. [19]Duke Cancer Institute, Duke University School of Medicine, Durham, NC, USA. [20]Preston Robert Tisch Brain Tumor Center, Duke University School of Medicine, Durham, NC, USA. [21]These authors contributed equally: Yoon-Mi Chung, Daniel J. Silver, Yue Hao. ✉e-mail: lathiaj@ccf.org

male individuals[1,12]. Consequently, substantial effort has been made to identify the underlying mechanisms of this effect, including tumour-intrinsic[13,14] and tumour microenvironment factors[15–17]. Androgen signalling has been reported to promote GBM growth by enhancing proliferation, migration and invasion in vitro[18–20]. By contrast, loss of androgen signalling inhibits tumour growth in immunodeficient mice and in non-orthotopic transplantation mouse models[19,20]. On the basis of these findings, AR blockade has been suggested as a potential therapy for GBM. However, the comprehensive effect of androgens on GBM, especially the involvement of the immune compartment and organ-specific microenvironments, has not been fully addressed.

Androgens have a crucial role in the sexual differentiation of the brain, particularly during the prenatal period[21], which is more prominent compared with that of almost all other non-reproductive organs. Androgen signalling masculinizes the male brain by guiding the development of male-typical neural structures and functions that regulate behavioural characteristics of male individuals[21,22]. Furthermore, owing to the high and regionally variable expression of aromatase, an enzyme that converts androgens to oestrogen, androgen signalling in the brain is uniquely regulated compared with other organs[23,24]. Considering the distinctive nature of androgen signalling in the brain, it is probable that androgen signalling contributes in some capacity to the sex differences observed in brain tumours, including GBM. Here we explore the role of androgens in antitumour immunity in GBM. We show that in combination with the loss of AR signalling, brain tumours specifically regulate immune responses via the hypothalamus–pituitary–adrenal (HPA) axis. Moreover, our findings demonstrate that androgens function as an immune-based tumour suppressor in brain tumours through mechanisms involving neuroinflammation. Together, our results highlight the distinct immune microenvironment of the brain.

Androgen loss shortens survival

We previously demonstrated a male-biased increase in T cell exhaustion in GBM that contributes to worse outcomes in male patients[16]. To further understand the sex differences in antitumour immunity that occur with ageing, we analysed T cell abundance in tumour samples obtained from 58 patients with high-grade gliomas (22 women, 36 men) using image-localized biopsy samples[25]. Bulk RNA sequencing (RNA-seq) of tumour samples was performed, and data were deconvolved to estimate T cell abundance in each sample. As there were multiple samples per patient, the average value of the T cell abundance per patient was obtained and presented for statistical analyses. Samples from male patients older than 50 years at diagnosis showed a significant decrease in T cell abundance compared with patients younger than 50 years (Extended Data Fig. 1a). By contrast, age did not show a significant effect on T cell abundance in samples from female patients (Extended Data Fig. 1b). Although multiple biological processes can exert age-dependent effects on tumour progression[26], we were particularly interested in whether the gradual reduction in sex hormones with ageing plays a part[27]. Thus, we questioned whether the decreased androgen levels in male individuals affect antitumour immunity in brain tumours.

To investigate the effect of androgens in brain tumour progression, 5-6-week-old male mice were surgically castrated and survival was analysed following intracranial implantation of various mouse syngeneic GBM models: SB28, GL261, CPA and KR158. Unlike other tumour models in which castration increased survival[3,4,28], castrated mice with GBM tumours exhibited significantly reduced survival compared with the sham-surgery group (Fig. 1a and Extended Data Fig. 2a) and the tumours were larger in size (Fig. 1b). Moreover, in a genetically engineered mouse model (GEMM) of GBM generated via electroporation of oncogenic plasmid DNA into the neonatal brain[29,30], we observed a similar accelerated tumour growth with reduced median survival in castrated mice (Extended Data Fig. 2b). These findings indicated that androgens suppress the growth of brain tumours, which prompted us to question whether this is a tumour-cell-specific or site-specific effect. To address this question, we intracranially implanted non-GBM cancer cells, either bladder cancer (MB49) or melanoma (B16-F10), into mice. For these two cells lines, androgens have been shown to have immunosuppressive and tumour-promoting roles[3,4]. In both these tumour models, we observed shortened survival in castrated mice (Fig. 1c), which suggested that the tumour-suppressive role of androgens is site-specific and not cell-type-specific. Furthermore, when mouse GBM cells (SB28) were subcutaneously implanted, tumour growth was delayed in the castration group (Fig. 1d), a result that aligns with previous reports of other tumours[3,4] and supports the brain-specific effect of androgens. Collectively, these results suggest that loss of androgens has a distinct role in controlling tumour growth in the brain.

To confirm that the decreased survival observed in castrated mice with brain tumours is an androgen-dependent effect, we treated gonadally intact male mice (8–9 weeks old) with enzalutamide, an AR inhibitor widely used in prostate cancer treatment[31]. Enzalutamide-treated mice showed decreased survival compared with the vehicle-treated group (Fig. 1e), which suggested that AR signalling mediates this survival difference. Furthermore, administration of exogenous testosterone extended survival in castrated mice, rescuing the decrease in survival observed with castration (Fig. 1f).

Notably, administration of exogenous testosterone to gonadally intact male mice further prolonged survival (Fig. 1g). To evaluate the clinical relevance of these findings, we analysed data from patients with GBM from the Surveillance, Epidemiology, and End Results (SEER) database (Fig. 1h). Survival analysis revealed that men with GBM who received both supplemental testosterone and temozolomide ($n = 61$, median overall survival (mOS) = 16 months) had significantly longer survival ($P < 0.001$) compared with individuals treated with temozolomide alone ($n = 1{,}272$, mOS = 12 months) (Fig. 1i). Hazard ratio (HR) analysis showed that men with GBM who received both supplemental testosterone and temozolomide had a 38% reduced risk of death (HR = 0.62, 95% confidence interval (CI) = 0.48–0.82, $P < 0.001$) compared with individuals who received temozolomide alone. In the fully adjusted model, the risk reduction increased to 34% (HR = 0.66, 95% CI = 0.50–0.86, $P = 0.003$). Together, these findings indicate a potential protective role for testosterone in GBM, which is in contrast to its effects in tumours outside the brain.

Tumour-extrinsic role of androgens in GBM

To assess the direct effects of androgens on GBM growth, we used in vitro and immunodeficient in vivo models. As previously shown[18–20], the addition of testosterone cypionate to mouse GBM cell cultures increased tumour cell number (Extended Data Fig. 2c), and both GBM models (SB28 and GL261) expressed high levels of AR (Extended Data Fig. 2d). Moreover, in immunodeficient NSG mice intracranially injected with GBM cells, tumour growth was delayed in castrated mice compared with the sham-surgery group (Extended Data Fig. 2e). Thus, these data suggest that androgen signalling promotes GBM tumour growth in the absence of an immune compartment.

Next, we sought to understand the mechanistic basis for the castration-mediated acceleration of brain tumour growth in immunocompetent mice. First, we assessed the impact of androgens on tumour growth. Immunofluorescence analyses showed that androgen depletion via castration did not influence tumour cell proliferation, as assessed by measuring phosphorylated histone H3 levels (Extended Data Fig. 3a). Moreover, RNA-seq of tumour tissues showed minimal gene expression changes between castrated and sham-surgery mice (Extended Data Fig. 3b and Supplementary Table 1). Notably, Gene Ontology (GO) term analysis showed that pathways related to cellular biosynthesis were downregulated in tumours from castrated mice (Extended Data Fig. 3c). These results prompted us to question whether

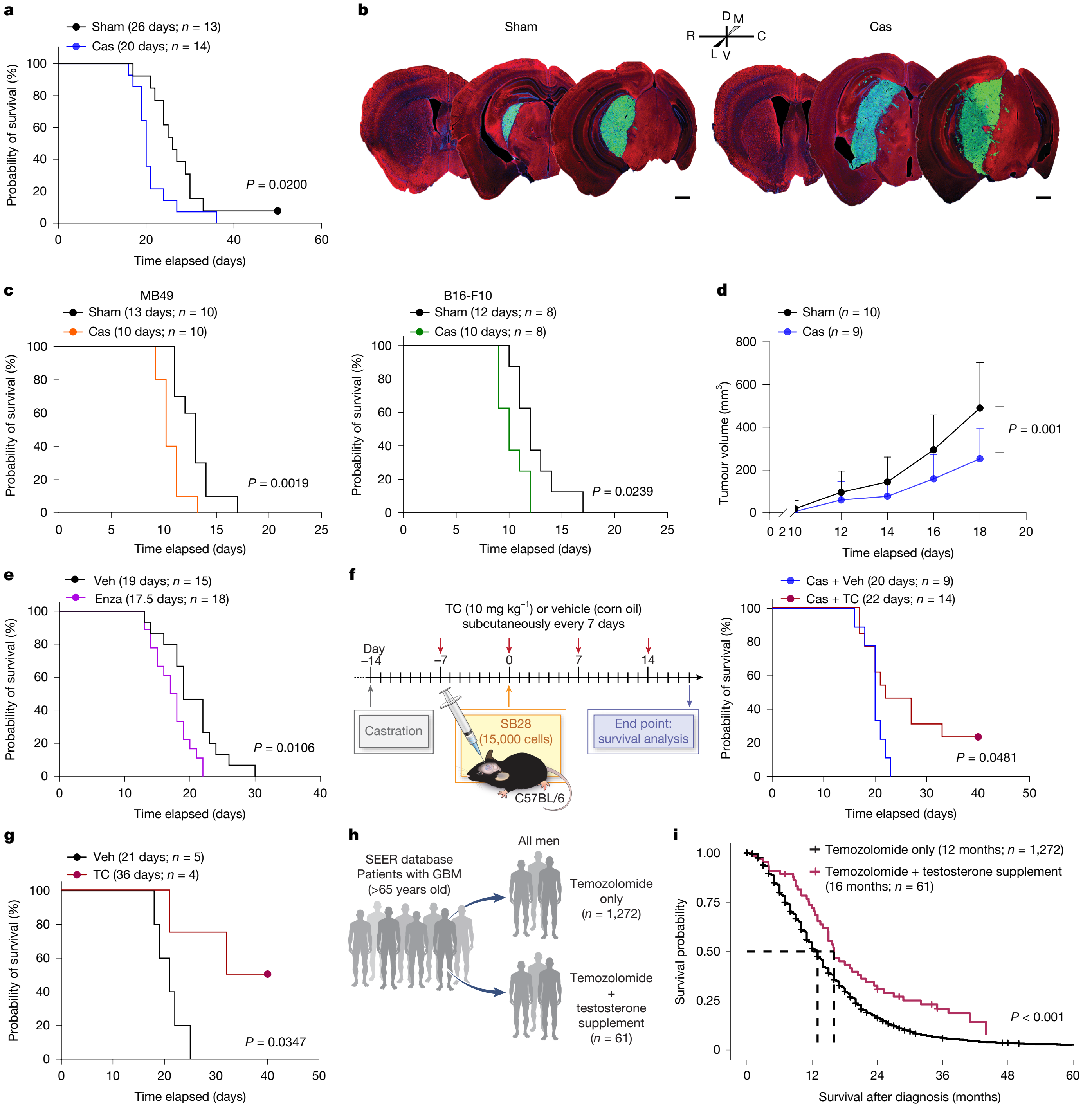

Fig. 1 | Loss of testosterone leads to shortened survival of mice with brain tumours in an androgen-dependent manner. **a**–**f**, Male mice aged 5–6 weeks old were castrated (Cas) or underwent a sham operation at least 2 weeks before tumour implantation. The median survival time and number of mice are indicated. Data were combined from two (**c**,**d**,**f**) or three (**a**,**e**) independent experiments. **a**, Survival analysis of B6 mice after intracranial implantation of SB28 tumours. **b**, Histology of mouse brain tissue 14 days after tumour implantation. Tubulin (red), eGFP (SB28, green), nuclei (Hoechst, blue). Scale bar, 1 mm. The anatomic rosette indicates the dorsal (D), ventral (V), rostral (R), caudal (C), medial (M) and lateral (L) directional axes. **c**, Survival analysis of B6 mice after intracranial implantation of MB49 or B16-F10 tumours. **d**, Tumour growth curve of B6 mice subcutaneously inoculated with SB28 tumours in the flank. **e**, Survival analysis of B6 male mice intracranially implanted with SB28 tumours after enzalutamide (Enza) or vehicle (Veh) treatment. **f**,**g**, Survival analysis of castrated (**f**) or gonadally intact (**g**) B6 male mice intracranially implanted with SB28 tumours and treated with testosterone cypionate (TC) or vehicle as depicted. The schematic in **f** shows the experimental schedule. **h**,**i**, Survival analysis of data from patients with GBM from the SEER-Medicare database (2008–2019). **h**, Schematic of the data analysis. **i**, Adjusted Kaplan–Meier curves by treatment group. Median survival time and number of patients in each group are indicated. Data are the mean ± s.d (**d**). Statistics: log-rank (Mantel–Cox) test (**a**,**c**–**g**), two-way analysis of variance (ANOVA) analysis (**d**) or multivariable Cox proportional hazards model (**i**). Illustrations in **f** and **h** reproduced with permission, Cleveland Clinic Foundation ©2026.

tumour growth differences are mediated by cell death. Staining for cleaved caspase-3, a marker for apoptotic cell death, revealed reduced cell death in tumours from castrated mice (Fig. 2a). This result suggests that impaired antitumour immunity may underlie the increase in tumour burden. Together, these data highlight a crucial role for tumour-extrinsic, immune-mediated mechanisms in modulating GBM growth following androgen depletion.

Castration induces T cell dysfunction

To further investigate the role of immune cells, we used *Rag1*$^{-/-}$ mice, which lack mature T cells and B cells, as a model. The castration-related effect on survival was abrogated in *Rag1*$^{-/-}$ mice after intracranial implantation of GBM cells (Fig. 2b and Extended Data Fig. 4a). This result suggests that adaptive immunity and lymphocytes have a crucial role in the castration-mediated effects on survival.

Immune cell analyses revealed that the production of antitumour cytokines such as IFNγ and TNF was significantly decreased in castrated mice, not only in tumour-infiltrating T cells (Fig. 2c, Extended Data Fig. 4b and Supplementary Fig. 1) but also in peripheral lymphoid organs such as lymph nodes (Fig. 2d) and spleen (Extended Data Fig. 4c). No difference in the frequencies of immune cell subsets infiltrated into the tumour was observed (Extended Data Fig. 4d). This decreased T cell function could explain the accelerated tumour growth and decreased cell death observed in castrated mice. These findings are in contrast to previous observations in other solid tumours, in which enhanced T cell function was observed with surgical castration[3,4,28]. Indeed, in mice that received a subcutaneous implantation of GBM cells in the flank, castration resulted in either comparable or increased T cell function in tumours (Fig. 2e), with elevated CD8^{+} T cell tumour infiltration (Extended Data Fig. 4e). Notably, in mouse models that had tumours implanted in either the brain or the flank, a decreased frequency of progenitor exhausted T cells was observed in castrated mice (Fig. 2f,g). This result supports previous findings of AR-mediated regulation of TCF1 transcription[4]. By contrast, terminally exhausted T cells and effector T cells showed different changes between brain tumours and flank tumours following castration (Fig. 2f,g). The terminally exhausted T cell population was increased in castrated mice with brain tumours, whereas effector T cells were decreased in brain tumours but increased in flank tumours.

These data indicate that there are additional mechanisms that regulate T cell function in brain tumours, beyond those mediated by androgens, in castration conditions. Collectively, these results demonstrate that loss of androgens induces systemic T cell dysfunction in a brain-tumour-specific manner that ultimately affects tumour growth.

Androgen loss increases HPA activity

Our findings thus far show that androgens function to constrain brain tumour growth. This phenotype is opposite to what has been observed in other solid tumours outside the brain. Given the systemic immunosuppression we observed, and acknowledging the well-established role of stress hormones, such as glucocorticoids, in decreasing T cell function[32], we investigated whether these effects could be attributed to changes in endogenous glucocorticoid levels. Indeed, liquid chromatography and tandem mass spectrometry (LC–MS/MS) analyses of serum from castrated mice revealed a significant increase in both corticosterone (CCT), an active form of glucocorticoid, and its inactive form, 11-dehydrocorticosterone (11-DHC) (Fig. 3a). Notably, the increase in CCT was observed regardless of brain tumour presence, whereas 11-DHC was further increased by the presence of a tumour in castrated mice (Fig. 3a). However, glucocorticoid levels were not increased in the brain tissue of castrated mice (Extended Data Fig. 5a). The decreased testosterone level in castrated mice was confirmed by MS analyses (Extended Data Fig. 5b,c). After AR blockade with enzalutamide, the serum concentration of glucocorticoids and testosterone was not altered (Extended Data Fig. 5d,e). However, the ratio of the active to inactive form (CCT/11-DHC) was significantly increased in mice in which ARs were blocked (Extended Data Fig. 5d). This result is consistent with previous reports in patients with prostate cancer treated with enzalutamide[33]. These data suggest that an additional mechanism that regulates glucocorticoid metabolism is altered after pharmacological blockade of ARs.

Next, we investigated whether an increase in glucocorticoid levels contributes to the shortened survival time of castrated mice. To that end, we blocked glucocorticoid receptor (GR; encoded by *Nr3c1*) function during tumour progression using mifepristone. Castrated mice treated with mifepristone showed significantly extended survival compared with the vehicle-treated group (Fig. 3b). However, this treatment effect was not observed in the sham-surgery group (without castration) (Fig. 3c). Immune cell analysis revealed that although GR inhibition did not alter immune cell infiltration into tumours, it enhanced cytokine expression in T cells (Extended Data Fig. 5f,g). These results suggest that an increase in castration-induced glucocorticoid levels promotes tumour progression by attenuating antitumour immunity.

Glucocorticoid production is tightly controlled by the neuroendocrine system via the HPA axis[34]. As the production of glucocorticoids in the adrenal gland is regulated by adrenocorticotropic hormone (ACTH) produced by the pituitary gland, we measured ACTH levels in the serum. In mice without tumours, there was no difference between sham-surgery and castration groups. By contrast, there was a significant increase in ACTH levels in castrated mice with brain tumours (Fig. 3d and Extended Data Fig. 5h). This increase in ACTH levels manifested acutely 1 day after tumour implantation (Extended Data Fig. 5i). Furthermore, intracranial implantation of non-GBM cells led to similar increases in ACTH levels after castration, which indicated that this increase is not a tumour-specific but a site-specific effect (Fig. 3e). The increase in ACTH depended on AR signalling, as mice with a brain tumour and treated with an AR inhibitor also resulted in increased ACTH production (Fig. 3f). Furthermore, the increased production of ACTH was reversed by exogenous testosterone treatment in castrated mice (Fig. 3g). Notably, hypothalamic neural cell activity was increased in castrated mice (Fig. 3h), a result that supports the idea that there is hyperactivation of the HPA axis in castrated mice with brain tumours.

Alterations in AR signalling had different effects in female mice. Although exogenous testosterone significantly reduced survival in female mice with brain tumours, it did not affect ACTH levels (Extended Data Fig. 6a–c). Note that endogenous female sex hormones were not manipulated in these mice. Similarly, AR blockade had no effect on either survival or ACTH production in female mice (Extended Data Fig. 6d–f). These results suggest that although testosterone can confer a male-like phenotype in terms of tumour progression in female individuals, its effect on the HPA axis may be regulated by more complex mechanisms, including interactions among multiple sex hormones and sex-biased, tissue-specific regulations in the HPA axis.

Taken together, our data suggest that brain tumours induce hyperactivation of the HPA axis in the absence of androgen signalling in male mice, which may lead to decreased antitumour T cell immunity and to promote tumour progression.

GR signalling acts via myeloid cells

Next, we investigated the mechanisms of glucocorticoid-mediated immunosuppression in castrated mice with brain tumours. Macrophages exhibited high GR expression, and several immune cell subsets, including T cells, natural killer (NK) cells and macrophages, showed increased GR expression following castration (Extended Data Fig. 7a,b). Given that glucocorticoids can suppress effector T cell activity either directly through GRs or indirectly via regulatory T (T_{reg}) cells[34], we first tested the involvement of these pathways. However,

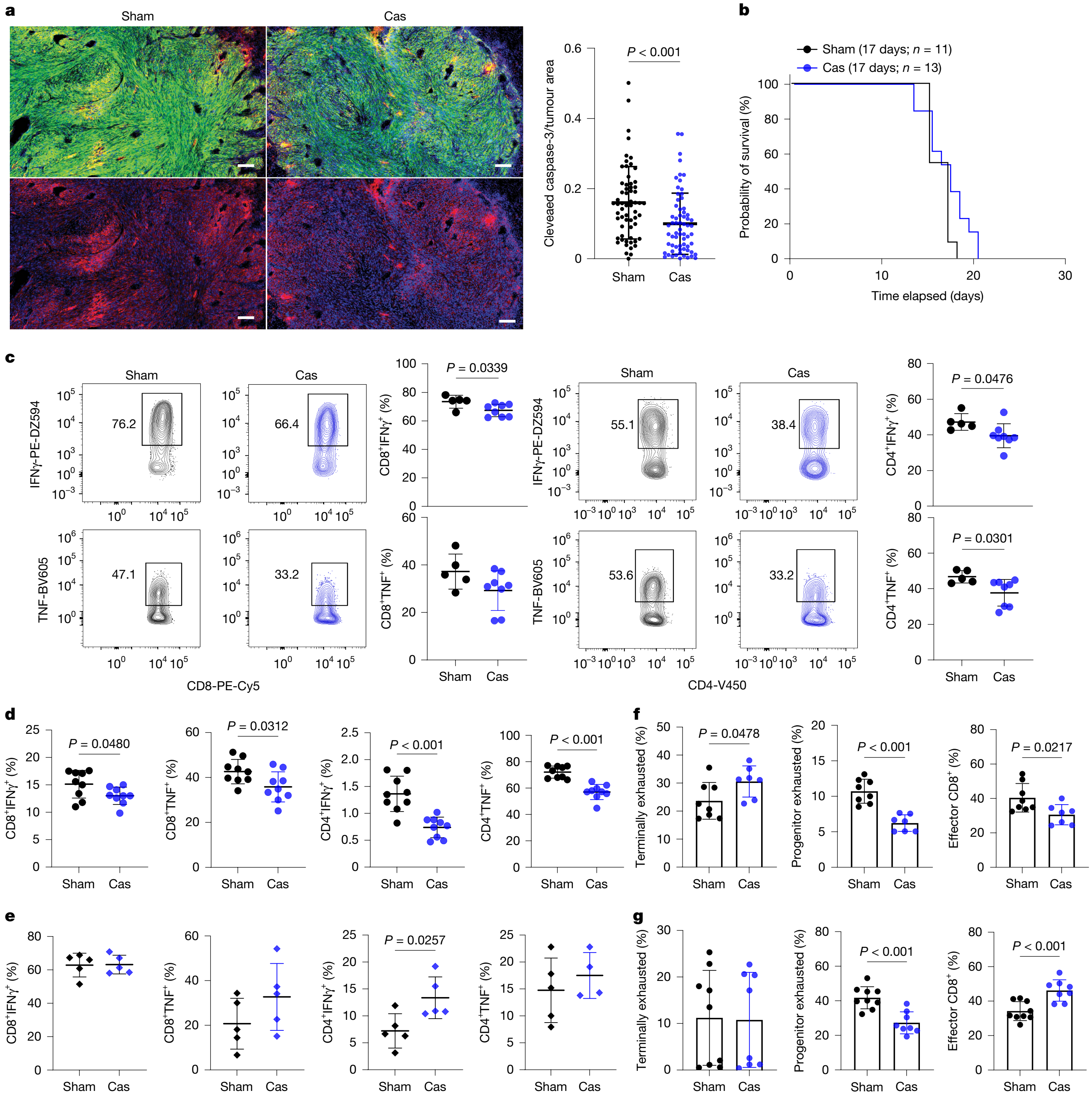

Fig. 2 | Castration induces a systemic attenuation of T cell function. **a**, Immunofluorescence analysis of tumour tissues from castrated mice and from sham-surgery mice (*n* = 5 per group) at day 14 after intracranial implantation of SB28 tumours. Left, representative images from sham-surgery mice and castrated mice with tumours. Cleaved caspase-3 (red), tumour (eGFP$^+$; green), nuclei (Hoechst; blue). Scale bars, 100 µm. Right, quantification of cleaved caspase-3 normalized to eGFP$^+$ tumour area. *P* = 0.000565. **b**, Survival analysis of *Rag1*$^{-/-}$ mice after intracranial implantation of SB28 tumours. Data were combined from four independent experiments. Median survival time and number of mice are indicated. **c**,**d**, Left, flow cytometry analysis of T cells obtained from sham-surgery mice and castrated mice 14 days after brain tumour (SB28) implantation. Right, cytokine production in T cells infiltrated into tumours (**c**) (*n* = 5 for sham, *n* = 8 for castrated) or inguinal lymph nodes (**d**) (*n* = 9 per group) was measured after 4 h of incubation with stimulation cocktail. *P* = 0.000154 (CD4$^+$IFNγ$^+$), *P* = 0.000013 (CD4$^+$TNF$^+$). **e**, Cytokine production in T cells infiltrated into flank tumours (SB28; *n* = 5 per group) measured on day 19. **f**,**g**, Frequency of CD8$^+$ T cell subsets from brain tumours (**f**) (*n* = 8 for sham, *n* = 7 for castrated) or flank tumours (**g**) (*n* = 9 for sham, *n* = 8 for castrated). The following markers were used to identify T cell subsets: terminally exhausted, CD8$^+$CD44$^+$PD1$^+$TIM3$^+$TCF1$^-$; progenitor exhausted, CD8$^+$CD44$^+$PD1$^+$TIM3$^-$TCF1$^+$; effector, CD8$^+$CD44$^+$TIM3$^-$TCF1$^-$. Data were combined from two independent experiments. *P* = 0.000053 (**f**, progenitor exhausted), *P* = 0.000301 (**g**, progenitor exhausted) and *P* = 0.000742 (**g**, effector). Data are the mean ± s.d. (**a**,**c**–**g**); *n* indicates the number of biologically independent animals. Statistics: unpaired two-tailed *t*-test (**a**,**c**–**g**) or log-rank (Mantel–Cox) test (**b**).

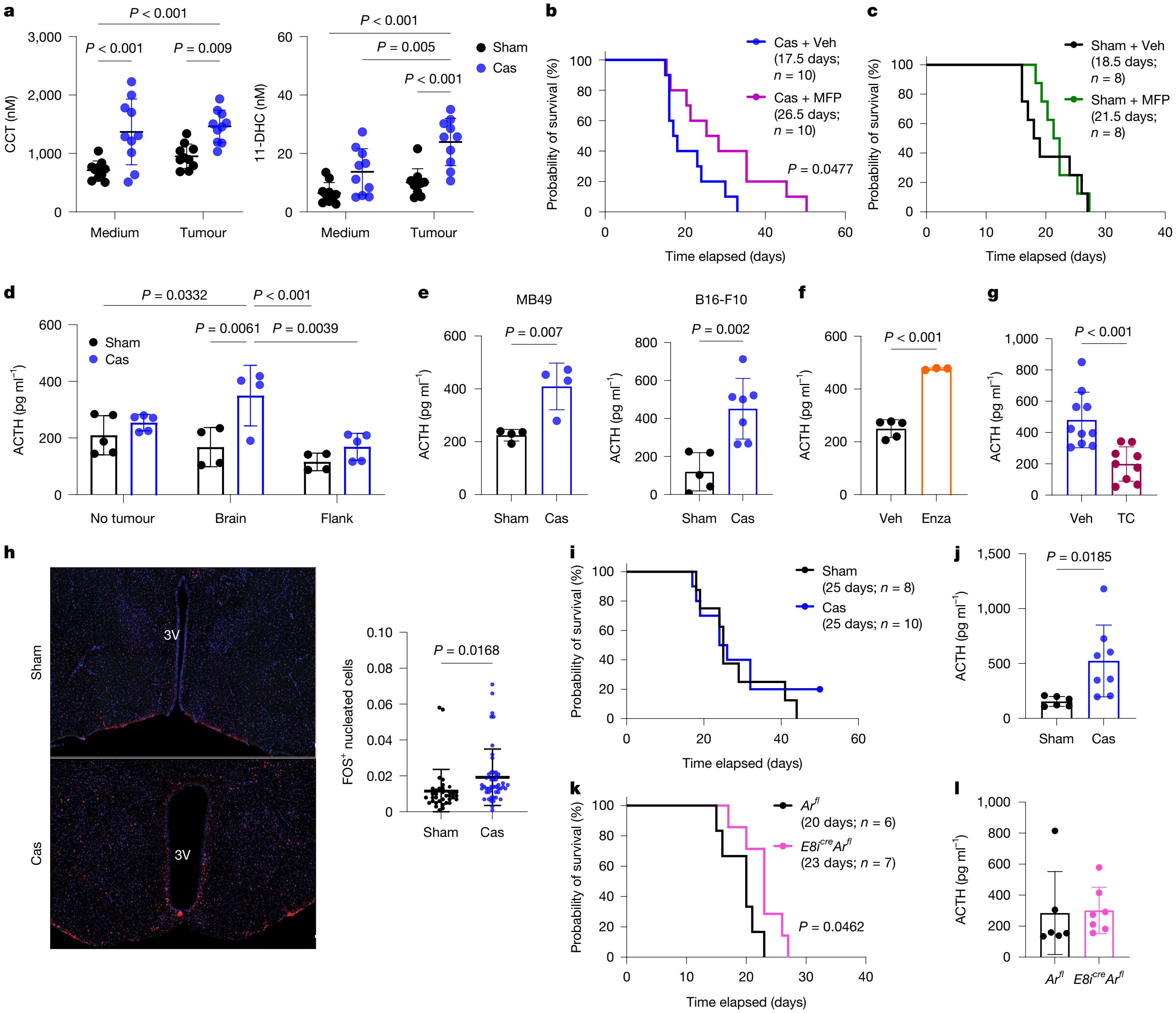

Fig. 3 | Activity of the HPA axis is increased in castrated mice with brain tumours. a, Mouse serum was collected 14 days after intracranial injection of tumour (SB28) or culture medium, and CCT and 11-DHC levels were measured by MS. $n = 10$ per group. $P = 0.000661$ (CCT; medium + sham versus castrated), $P = 0.000102$ (CCT; medium + sham versus tumour + castrated), $P = 0.000003$ (11-DHC; medium + sham versus tumour + castrated), $P = 0.000127$ (11-DHC; tumour + sham versus castrated). **b**,**c**, Survival analysis of castrated mice (**b**) and sham-surgery mice (**c**) with SB28 (brain) tumours treated with mifepristone (MFP) or vehicle. Median survival time and number of mice are indicated. Data were combined from two independent experiments. Experiments for castration (**b**) and sham-surgery (**c**) mice were performed separately. **d**, Serum ACTH levels were measured using ELISA. Serum was collected 14 days (brain) or 20 days (flank) after SB28 tumour implantation or from tumour-free mice. $n = 4$ per group for brain tumour + sham, brain tumour + castration, flank tumour + sham; $n = 5$ per group for no tumour + sham, no tumour + castration, flank tumour + castration. $P = 0.000415$ (brain + castration versus flank tumour + sham). **e**, Serum ACTH levels were measured at the end point after intracranial implantation with MB49 ($n = 4$ per group) or B16-F10 ($n = 5$ for sham, $n = 7$ for castrated) tumours. **f**, Serum ACTH levels in gonadally intact SB28-bearing (brain) mice treated with vehicle or enzalutamide. Serum samples were collected at the end point. $n = 5$ for vehicle, $n = 3$ for enzalutamide. $P = 0.00003$. **g**, Serum ACTH levels at the end point from castrated SB28-bearing (brain) mice treated with vehicle (corn oil) or TC. $n = 10$ for vehicle, $n = 9$ for TC. Data were combined from two independent experiments. $P = 0.000760$. **h**, Neural activity in the hypothalamus of mice with brain tumours (SB28, day 14). Left, representative images. FOS (red), nuclei (Hoechst; blue). Scale bar, 100 µm, 3V, third ventricle. Right, quantification of FOS^{+} nucleated cells in the hypothalamus. $n = 5$ for sham, $n = 7$ for castrated. **i**, Survival analysis of *LysM*^{cre}*Nr3c1*^{fl} mice intracranially implanted with SB28 tumours after sham or castration surgery. Data are combined from two independent experiments. Median survival length and number of mice are indicated in the graph. **j**, Serum ACTH levels in *LysM*^{cre}*Nr3c1*^{fl} mice with brain tumours (SB28) euthanized on day 16. $n = 6$ for sham, $n = 8$ for castrated. **k**, Survival analysis of *E8i*^{cre}*Ar*^{fl} mice intracranially implanted with SB28 tumors. Data are combined from two independent experiments. Median survival length and number of mice are indicated in the graph. **l**, Serum ACTH levels measured at the end point in *E8i*^{cre}*Ar*^{fl} mice from **k**. $n = 6$ for *Ar*^{fl}, $n = 7$ for *E8i*^{cre}*Ar*^{fl}. Data are the mean ± s.d.; n indicates the number of biologically independent animals. Statistics: two-way ANOVA analysis with Tukey's multiple comparison test (**a**,**d**), log-rank (Mantel–Cox) test (**b**,**c**,**i**,**k**) or unpaired two-tailed t-test (**e**–**h**,**j**,**l**).

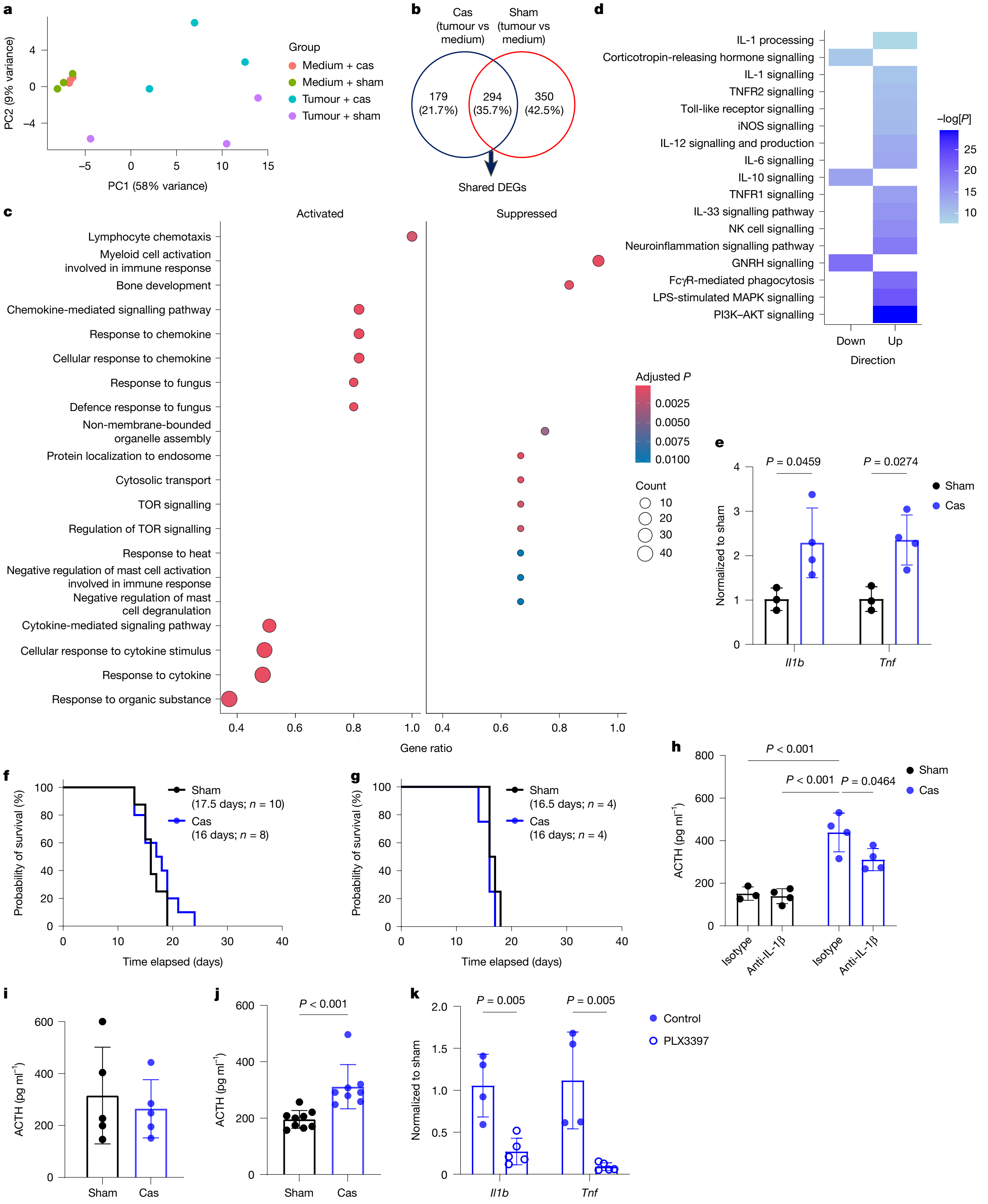

Fig. 4 | See next page for caption.

Fig. 4 | Castration enhances HPA axis activation via increased proinflammatory cytokine signalling in brain tumours. a–**c**, RNA-seq analysis of hypothalamus samples from castrated mice and sham-surgery mice at day 14 after intracranial injection of SB28 tumour cells or culture medium. $n = 3$ per group. **a**, PCA plot. **b**, Shared DEGs between castrated and sham-surgery groups. **c**, GO term enrichment analysis of shared DEGs from **b**. **d**, Phosphorylation array of hypothalamus samples from castrated mice and sham-surgery mice on day 14 after intracranial injection of SB28 tumours. Heatmap shows canonical pathway analysis based on phosphorylated proteins comparing castration and sham-surgery groups. **e**, mRNA expression levels in brain tumour (SB28) tissue from sham-surgery mice and castrated mice at day 7 after intracranial injection. $n = 3$ for sham, $n = 4$ for castrated. **f**,**g**, Survival analysis of *Il1r1*$^{-/-}$ (**f**) and *Tnfr1/2*$^{-/-}$ (**g**) mice intracranially implanted with SB28 tumours following sham or castration surgery. Median survival time and number of mice are indicated. Data were combined from three independent experiments (**f**). **h**, Serum ACTH levels in brain tumours (SB28) from the indicated mice measured on day 7 after isotype or anti-IL-1β antibody treatment. $n = 4$ per group except for $n = 3$ for sham + isotype. **i**, Serum ACTH levels measured on day 3 after intracranial implantation of SB28 tumours in *Tnfr1/2*$^{-/-}$ mice treated with anti-IL-1β antibody. $n = 5$ per group. **j**, Serum ACTH levels measured on day 3 after intracranial injection of SB28 lysates. $n = 9$ for sham, $n = 8$ for castrated. Data were combined from two independent experiments. **k**, mRNA levels in brain tumour tissue from castrated mice on day 7 after intracranial implantation of SB28 cells following microglia depletion via a PLX3397-supplemented diet. $n = 4$ for control, $n = 5$ for PLX3397. Data are the mean ± s.d. *n* indicates the number of biologically independent animals. Statistics: one-sided permutation test (**c**), right-tailed Fisher's exact test (**d**), multiple unpaired *t*-test (**e**,**h**), log-rank test (**f**,**g**), two-way ANOVA analysis with Tukey's multiple comparison test (**h**) or unpaired two-tailed *t*-test (**i**,**j**).

the castration-related effects on survival and ACTH production were not altered in T cell-specific *Nr3c1* knockout (KO) (*Lck*^{cre}*Nr3c1*^{fl}) or T_{reg} cell-specific *Nr3c1* KO (*Foxp3*^{cre}*Nr3c1*^{fl}) strains (Extended Data Fig. 7c–f). Previous studies have shown that glucocorticoid-induced immunosuppression can be mediated by macrophages[35,36]. Notably, specific deletion of *Nr3c1* in myeloid cells (*LysM*^{cre}*Nr3c1*^{fl}) abolished the castration effect on survival (Fig. 3i) despite increased ACTH production (Fig. 3j). In these *LysM*^{cre}*Nr3c1*^{fl} mice, cytokine expression in T cells was comparable between castrated and sham-surgery control groups (Extended Data Fig. 7g). These findings indicate that the suppressive activity of glucocorticoids is mediated by GR-expressing myeloid cells, such as macrophages, in the tumour. Moreover, T cells in the periphery exhibited attenuated cytokine expression in castrated *LysM*^{cre}*Nr3c1*^{fl} mice (Extended Data Fig. 7h,i), which suggests that there is a site-specific mechanism of glucocorticoid-mediated immune suppression.

We next evaluated the role of AR signalling in CD8$^+$ T cells in our brain tumour model using a CD8$^+$ T cell-specific *Ar* KO (*E8i*^{cre}*Ar*^{fl}) strain. Consistent with previous reports of non-brain tumour models[3,4], *E8i*^{cre}*Ar*^{fl} mice exhibited prolonged survival compared with littermate controls (*Ar*^{fl}) following intracranial tumour implantation (Fig. 3k). Notably, this improvement in survival was not accompanied by changes in ACTH levels (Fig. 3l). Castration did not change survival times of *E8i*^{cre}*Ar*^{fl} mice with brain tumours (Extended Data Fig. 7j) despite increased ACTH levels (Extended Data Fig. 7k), which indicated that there is a complex interplay between androgen and glucocorticoid-mediated immune regulation. These results suggest that the increased brain tumour growth observed in castrated mice cannot be solely explained by AR signalling loss in CD8$^+$ T cells. Thus, there is a distinct brain-tumour-specific mechanism involving glucocorticoid-mediated immunosuppression.

To better understand how castration affects immune responses in our brain tumour model, we performed single-cell RNA sequencing (scRNA-seq) of CD45$^+$ immune cells isolated from tumours and spleens of castrated and sham-surgery mice. Clustering analysis confirmed that there is no difference in immune cell subsets between these groups (Supplementary Table 2 and Supplementary Fig. 2a,b). Similarly, subclustering of the T cell population did not show major changes between the groups (Supplementary Table 3 and Supplementary Fig. 2c,d). Gene set enrichment analysis (GSEA) indicated that the corticosterone response pathway is more enriched in tumour-infiltrating CD8$^+$ T cells from castrated mice. By contrast, this pathway was more prominent in tumour-associated macrophages and splenic myeloid dendritic cells in the sham-surgery group (Extended Data Fig. 8a). This result suggests that increased glucocorticoid levels exert distinct effects across immune cell subsets.

CellChat analysis revealed that castration alters immune cell–cell communication in both the tumour and splenic microenvironments. In tumours, castration reduced the total number of interactions but increased the overall interaction strength, which indicated that fewer interactions occur but there is stronger signalling among immune cells (Supplementary Fig. 2e). By contrast, in the spleen, castration increased the number of interactions while reducing their average strength (Supplementary Fig. 2e). Effector CD8$^+$ T cells emerged as the primary targets of immune communication, whereas myeloid cells, such as cells expressing interferon-stimulated genes, macrophages and myeloid dendritic cells, serve as prominent sources of these signals (Extended Data Fig. 8b). Pathway-level analysis showed that immune cells in tumours from castrated mice were enriched for immunosuppressive signalling pathways (CD200, CD96, CD52, adenosine, CD39 and macrophage migration inhibitory factor (MIF)), whereas those from the sham-surgery group were enriched for pro-inflammatory pathways (TNF, osteopontin (also known as SPP1), 2-arachidonoylglycerol and cyclophilin A) (Supplementary Fig. 2g). These differences were more evident in the spleen (Supplementary Fig. 2h).

Ligand–receptor analysis further indicated that these myeloid cells communicate with effector CD8$^+$ T cells via integrins, secreted factors, major histocompatibility complex (MHC) class I molecules and co-receptors in both tumours and the spleen (Extended Data Fig. 8c and Supplementary Fig. 2i). Notably, the probability of MHC class I–CD8 interactions and inhibitory receptor–ligand interactions such as PD1 (encoded by *Pdcd1*) and CTLA4 (encoded by *Ctla4*) was increased in castrated mice. This result suggests that there is enhanced myeloid–CD8$^+$ T cell immune synapse formation and increased immunosuppressive signalling in these mice. Reciprocal analysis of CD8$^+$ T cells to myeloid interactions revealed a strong MIF–CD74 interaction in the castration group. This result provides further support for enhanced immunosuppressive crosstalk in these mice given the suppressive role of this pathway in tumour microenvironments, including gliomas[37] (Extended Data Fig. 8d). Using GBM-associated myeloid cell signatures (GBmap)[38], we validated that myeloid cells in castrated mice exhibit decreased expression of pro-inflammatory gene signatures (Extended Data Fig. 8e).

Together, these results suggest that androgen deprivation reshapes immune cell communication networks towards a more immunosuppressive state, which contributes to impaired antitumour immunity in brain tumours.

Neuroinflammation mediates HPA activation

To understand how brain tumours induce increased activity of the HPA axis under an androgen-deprived setting, RNA-seq was performed on hypothalamus tissue isolated from castrated mice and from sham-surgery mice after intracranial injection with mouse GBM cells (SB28) or with culture medium. Principal component analysis (PCA) plots showed that samples from medium-injected mice clustered together regardless of castration condition, which suggests that brain tumours trigger transcriptional changes in the hypothalamus after androgen loss (Fig. 4a). Differentially expressed gene (DEG) analysis (Extended Data Fig. 9a and Supplementary Table 4) and GO

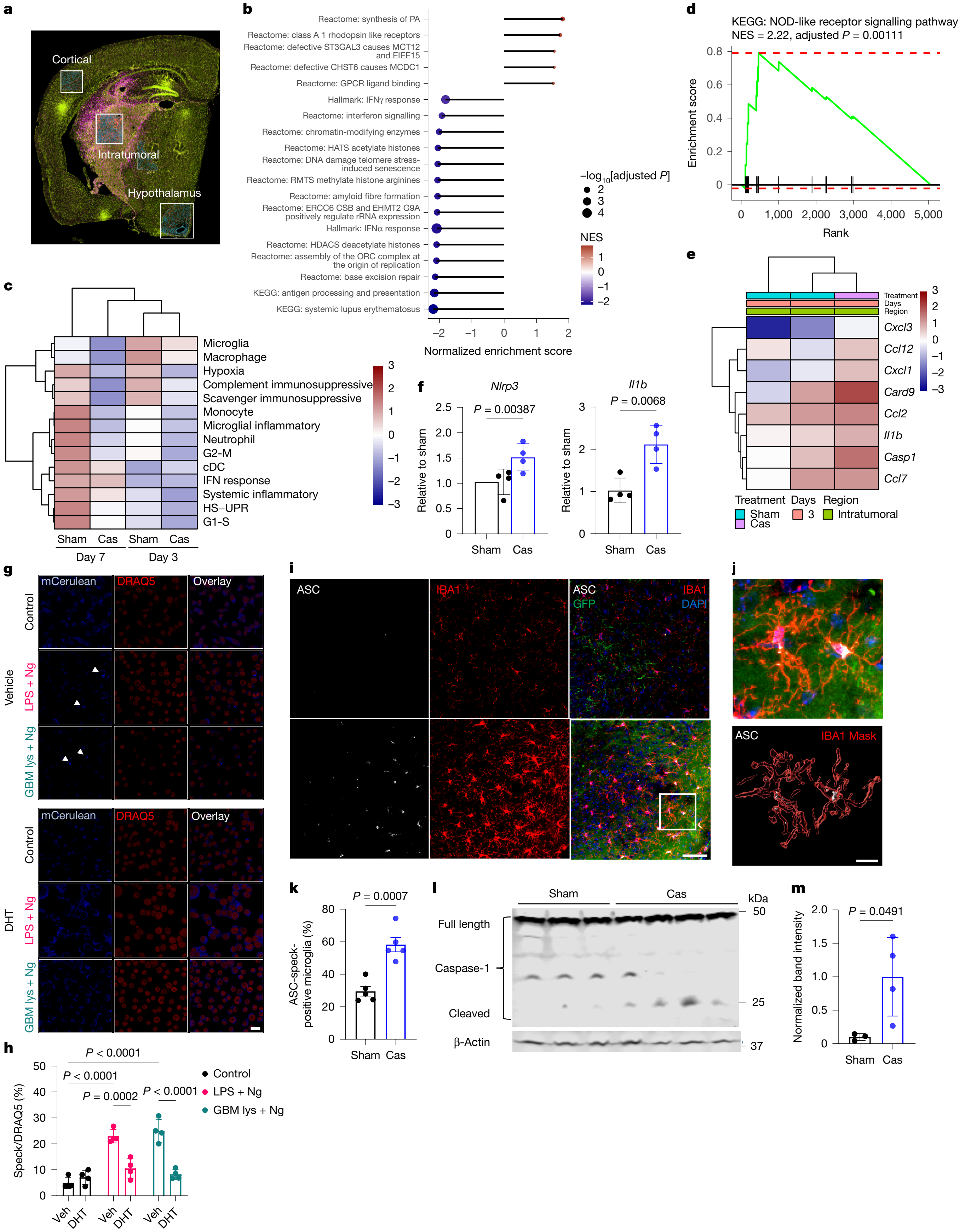

Fig. 5 | See next page for caption.

Fig. 5 | Enhanced neuroinflammation is mediated by increased microglial inflammasome activity in castrated mice with brain tumours. a–**e**, Spatial transcriptomics using Nanostring Digital Spatial Profiling was performed on brain tissue samples from sham-surgery mice and castrated mice on day 3 or 7 after tumour (SB28) implantation (n =3 per group). **a**, Representative image of ROIs. **b**, Pathway enrichment analysis of IBA1$^+$ cells across all ROIs and time points (castrated versus sham). **c**, Myeloid cell signatures in IBA1$^+$ cells from intratumoral regions. **d**, GSEA pathway analysis of IBA1$^+$ cells from intratumoral regions on day 3. **e**, Heatmap of the top-ranked genes in **d**. **f**, mRNA expression levels in tumour tissue samples from sham-surgery mice and castrated mice at day 3 after intracranial tumour (SB28) injection. $n = 4$ per group. **g**,**h**, In vitro ASC speck formation in ASC-mCerulean-overexpressing macrophages. After 72 h of DHT treatment (10 nM) or vehicle (methanol), cells were stimulated with LPS and nigericin (Ng), GBM (SB28) lysates and Ng (GBM lys + Ng) or left unstimulated (control). $n = 4$ per group. **g**, Representative image showing ASC specks (mCerulean; blue) and nuclei (DRAQ5; red). Arrows indicate ASC specks. Scale bar, 20 µm. **h**, Quantification of speck-positive cells. **i**–**k**, In vivo ASC speck formation in IBA1$^+$ microglia in brain tissues from sham-surgery mice and castrated mice with brain tumours (SB28) at day 3 after tumour implantation. $n = 5$ per group. **i**, Representative images from sham-surgery mice and castrated mice with tumours. ASC (white), IBA1 (red), SB28 tumour (GFP; green), nuclei (DAPI; blue). Scale bar, 50 µm. **j**, Magnified image of box shown in **i** and 3D reconstruction showing ASC specks inside IBA1$^+$ microglia. Scale bar, 10 µm. **k**, Quantification of speck-positive cells. **l**,**m**, Immunoblot analysis of mouse brain tissue lysates for caspase-1. **l**, Representative blot, **m**, Quantification of cleaved caspase-1 (p20 subunit). $n = 3$ for sham, $n = 4$ for castrated. Data are the mean ± s.d. Statistics: permutation test (**b**,**d**), unpaired two-tailed t-test (**f**,**k**,**m**) or two-way ANOVA analysis with Tukey's multiple comparison test (**g**).

term analysis showed that gonadotropin secretion and development processes were increased in the hypothalamus of castrated mice with tumours compared with sham-surgery mice with tumours (Extended Data Fig. 9b). To assess the impact of brain tumours on the hypothalamus, we first identified DEGs by comparing tumour-injected and medium-injected mice in each group (sham or castrated). We then identified 294 shared DEGs that were consistently altered by tumour presence across both conditions (Fig. 4b). GO term analysis showed that these shared DEGs are enriched in the pathways related to cytokine responses (Fig. 4c), which indicated that brain tumours promote inflammatory responses in the hypothalamus.

As cytokine signalling involves multiple phosphorylation events across various pathways, phosphorylation array analysis was performed on hypothalamic tissue from castrated mice and sham-surgery mice with brain tumours. This analysis identified 108 differentially phosphorylated proteins between the two groups (78 upregulated and 30 downregulated in the castration group) (Extended Data Fig. 9c and Supplementary Table 5). Pathway enrichment analysis revealed that these differentially phosphorylated proteins are associated with proinflammatory cytokine signalling, which were increased in the hypothalamus of castrated mice (Fig. 4d). Upstream regulator analysis further predicted that TNF and IL-1β are key drivers of these phosphorylation changes (Supplementary Table 5).

Thus, results from both RNA-seq and phosphorylation array analyses point to heightened cytokine signalling in the hypothalamus of castrated mice with brain tumours. Previous studies have shown that proinflammatory cytokines can activate the HPA axis[39]. Consistent with this finding, *Il1b* and *Tnf* mRNA levels were significantly increased in the brains of castrated mice with tumours (Fig. 4e). To test whether these cytokines contribute to the castration-induced tumour-promoting effects, mouse strains lacking IL-1 receptor 1 (*Il1r1*$^{-/-}$) or TNF receptors 1 and 2 (*Tnfr1/2*$^{-/-}$) were castrated and implanted with brain tumours. Notably, castration did not affect survival in either strain, which suggests that IL-1β and TNF mediate the castration-mediated effects on brain tumour growth (Fig. 4f,g). ACTH levels measured at the end point showed a modest increase in castrated mice (Extended Data Fig. 10a,b). To circumvent possible developmental effects from germline KO models, we pharmacologically inhibited IL-1β signalling using an anti-IL-1β antibody. IL-1β blockade significantly reduced ACTH levels in castrated mice but had no effect in sham-surgery mice (Fig. 4h). Moreover, blocking both cytokine signalling pathways by treating *Tnfr1/2*$^{-/-}$ mice with an anti-IL-1β antibody completely abrogated ACTH production differences between the castrated and sham-surgery groups (Fig. 4i). Collectively, these findings indicate that increased proinflammatory cytokine signalling mediates HPA axis hyperactivation in castrated mice with brain tumours.

The increased cytokine expression observed in castrated mice occurred only when tumour cells were implanted and not in response to injection of medium or without any insult (Extended Data Fig. 10c). To further explore whether inflammatory triggers induce changes in ACTH production, we injected GBM cell lysates into the brain. As expected, castrated mice showed increased ACTH production (Fig. 4j) and *Il1b* mRNA expression was significantly increased (Extended Data Fig. 10d). This effect was not due to a mass effect, as implantation of latex beads, which are similar in size to tumour cells, reduced ACTH production in castrated mice (Extended Data Fig. 10e). Thus, the increase in ACTH and proinflammatory cytokine expression in castrated mice is induced by inflammatory stimuli.

Increased ACTH production and elevated *Il1b* and *Tnf* mRNA levels were also observed in immunodeficient NSG mice (Extended Data Fig. 10f,g), whereas ACTH production was similarly increased in *Rag1*$^{-/-}$ mice (Extended Data Fig. 10h). This result suggests that peripheral adoptive immune cells do not mediate the observed increase in HPA axis activity. A similar effect was observed in NSG mice injected with patient-derived GBM cells (L1 and GBM23) (Extended Data Fig. 10i), and *Il1b* mRNA levels were increased following castration (Extended Data Fig. 10j). Microglia, brain-resident immune cells, are critical mediators of innate immune responses to inflammatory insults. As NSG mice retain microglia, we proposed that microglia may mediate this increased neuroinflammatory response observed after castration. Consistent with this hypothesis, microglia depletion significantly reduced *Il1b* and *Tnf* mRNA expression (Fig. 4k and Extended Data Fig. 10k). These data support the role of microglia in driving elevated neuroinflammation in castrated mice with brain tumours.

Androgen signalling suppresses inflammasome activity

To further investigate the mechanisms that underlie microglia-mediated neuroinflammation, we performed spatial transcriptomic of brain tissue samples from castrated mice and sham-surgery mice at two time points: day 3 and day 7 after tumour implantation. Regions of interest (ROIs) included cortical, intratumoral and hypothalamus areas, and IBA1 was used to identify myeloid cell compartments (Fig. 5a). Comparisons of castrated and sham conditions in IBA1$^+$ and IBA1$^-$ cell compartments from all regions at both time points revealed significant transcriptional differences, particularly from the intratumoral regions (Supplementary Table 6 and Supplementary Fig. 3a–d). Pathway analysis of IBA1$^+$ cell compartments revealed that immune responses were downregulated in castrated mice, such as interferon signalling and related responses, and antigen processing and presentation (Fig. 5b). Similarly, pathway analysis of IBA1$^-$ non-myeloid cells showed that immune responses were downregulated in castrated mice (Supplementary Fig. 3e), a result consistent with our findings of dampened immune responses in brain tumours following castration. Next, we performed myeloid cell signature analysis of IBA1$^+$ cell compartments using published GBM-associated myeloid cell refs. 38,40 and found that these signatures were more enriched in intratumoral regions regardless of time points (Supplementary Fig. 3f). To detect castration-induced differences, data from intratumoral regions were re-scaled (Fig. 5c). On day 3, IBA1$^+$ myeloid cells from the sham-surgery group exhibited more enriched immunosuppressive phenotypes (complement and scavenger) compared with castrated mice. By contrast, on day 7, additional inflammatory signatures (microglial and systemic inflammatory) were also more prominent in the sham-surgery condition (Fig. 5c).

To understand how brain tumours initiate neuroinflammation, we focused on data from day 3, a time point early enough to capture innate immune responses. Notably, IBA1$^+$ myeloid cells showed increased NOD-like receptor (NLR) signalling pathway activation in castrated mice (Fig. 5d), and expression of top-ranked genes in this pathway was higher (Fig. 5e). NLRs sense danger signals from pathogens and cellular damage and initiate inflammatory responses through the inflammasome complex[41]. As brain tumours initiate neuroinflammatory responses through damage-associated molecular pattern (DAMP) signalling[42], we proposed that androgen loss heightens microglia-mediated responses to tumour-derived DAMP signals via the NLR–inflammasome pathway. Indeed, castrated mice exhibited increased expression of *Il1b* and *Nlrp3*, key components of the inflammasome pathway (Fig. 5f).

We next tested whether androgen signalling regulates inflammasome activity. We treated immortalized macrophages overexpressing ASC-mCerulean with dihydrotestosterone (DHT) in vitro, followed by stimulation with lipopolysaccharide (LPS) and nigericin, a positive control for inflammasome activation, or with mouse GBM cell lysates plus nigericin to model GBM-relevant DAMP signals. NLRP3 engagement culminates in the condensation of ASC-mCerulean expression into 'specks' (a marker of inflammasome activation)[43–45]. DHT treatment significantly reduced ASC speck formation, as analysed by confocal microscopy (Fig. 5g,h) and flow cytometry (Extended Data Fig. 10l), and decreased IL-1β secretion (Extended Data Fig. 10m). Next, we assessed inflammasome activation in vivo. Castration increased ASC speck formation in IBA1$^+$ microglia (Fig. 5i–k) and elevated cleaved caspase-1 levels (Fig. 5l,m), which indicated that there is enhanced inflammasome activation in castrated mice with brain tumours. Together, these findings indicate that androgen signalling suppresses inflammasome activation and neuroinflammation and that androgen loss amplifies tumour-associated inflammatory responses in the brain.

In summary, our data demonstrate that androgen loss drives distinct immunosuppressive mechanisms in brain tumours through elevated local neuroinflammation and hyperactivation of the neuroendocrine system to ultimately promote tumour progression (Supplementary Fig. 4).

Discussion

In this study, we demonstrated that androgens are important regulators of antitumour immunity in brain tumours and act through brain-specific mechanisms. Although immunotherapies have substantially improved treatment of certain cancers, clinical trials of immunotherapy for GBM have been unsuccessful. In addition to tumour-intrinsic factors such as high heterogeneity and low antigenicity, the immunologically cold aspect of GBM is partly attributed to its location, which includes the blood–brain barrier and the presence of brain-resident microglia and infiltrating immunosuppressive myeloid cells[46]. Therefore, understanding the distinct immune environment of the brain is crucial for the development of effective therapies for GBM. Recent publications in cancer immunology have highlighted the immunosuppressive role of androgens, showing that androgen signalling dampens antitumour T cell responses and reduces the efficacy of immune checkpoint inhibitors[3,4,11]. Here, our findings revealed that the loss of androgen signalling in the context of brain tumours leads to impaired antitumour immunity and worsened disease outcomes. Although our findings demonstrated that GR-mediated immune regulation is the key driver of castration-induced tumour progression, increased glucocorticoid may also directly regulate brain tumour growth in a circadian rhythm-dependent manner[47]. Considering the complexity of brain structures and their role in regulating various functions, our findings underscore the importance of understanding the brain-specific mechanisms in tumour immunobiology. Furthermore, understanding how androgen-deprivation therapy or testosterone supplementation affects non-reproductive organ cancers, and whether outcomes differ in the presence or absence of brain metastasis, remains a critical area for future clinical investigation.

The median age at diagnosis for GBM is 68–70 years old[48], an age that negatively affects patient survival[49]. Given that serum testosterone production in men decreases with age[27], it is important to consider how reduced androgen signalling may affect brain tumour progression. A similar trend is observed in multiple sclerosis, for which later disease onset in men coincides with declining testosterone levels, and lower androgen levels correlate with increased disease severity[50]. Our analysis of real-world data suggests that supplemental testosterone in older men (>65 years at the time of diagnosis) is associated with significant increases in survival after diagnosis with GBM (Fig. 1i). Although this survival benefit may involve multiple factors, such as anticachexia effects, the potential immunomodulatory role of testosterone warrants further investigation. A limitation of the current study involved the use of young male mice (5–6 weeks old), which does not reflect age-related changes in immune system and endocrine functions. Thus, future studies will focus on evaluating the effect of androgens on brain tumours in the context of ageing using appropriate animal models.

Although mouse GBM models, including GEMMs, cannot fully capture the complexity and heterogeneity of human GBM, they remain valuable for identifying mechanistic links. Our findings provide a framework to investigate how testosterone, neuroinflammation and immunomodulation intersect in human GBM. Meanwhile, patients with GBM are often treated with dexamethasone for oedema control, especially around the time of surgery and radiation therapy[51]. Dexamethasone potently suppresses inflammation, with durable immunosuppressive effects[40], and the HPA axis. Thus, the combined effect of decreased serum testosterone and dexamethasone requires further consideration in a clinical setting. Together, this work highlights the unique aspects of central nervous system immunity in response to androgen loss and illustrates how neuroendocrine regulation influences the antitumour immune response in the brain. Our results emphasize the importance of understanding brain tumour biology, considering its distinct anatomical and functional context. By uncovering sex-based immune mechanisms regulated by hormone signalling, our findings underscore the need to incorporate sex as a biological variable in brain tumour research that can potentially inform more personalized approaches to immunotherapy for brain tumours.

Online content

Any methods, additional references, Nature Portfolio reporting summaries, source data, extended data, supplementary information, acknowledgements, peer review information; details of author contributions and competing interests; and statements of data and code availability are available at https://doi.org/10.1038/s41586-026-10451-5.

1. Ostrom, Q. T., Rubin, J. B., Lathia, J. D., Berens, M. E. & Barnholtz-Sloan, J. S. Females have the survival advantage in glioblastoma. *Neuro. Oncol.* **20**, 576–577 (2018).
2. Xiao, T. et al. Hallmarks of sex bias in immuno-oncology: mechanisms and therapeutic implications. *Nat. Rev. Cancer* **24**, 338–355 (2024).
3. Yang, C. et al. Androgen receptor-mediated CD8$^+$ T cell stemness programs drive sex differences in antitumor immunity. *Immunity* **55**, 1268–1283 (2022).
4. Kwon, H. et al. Androgen conspires with the CD8$^+$ T cell exhaustion program and contributes to sex bias in cancer. *Sci. Immunol.* **7**, eabq2630 (2022).
5. Cook, M. B., McGlynn, K. A., Devesa, S. S., Freedman, N. D. & Anderson, W. F. Sex disparities in cancer mortality and survival. *Cancer Epidemiol. Biomarkers Prev.* **20**, 1629–1637 (2011).
6. Siegel, R. L., Miller, K. D. & Jemal, A. Cancer statistics, 2017. *CA Cancer J. Clin.* **67**, 7–30 (2017).
7. Abdel-Hafiz, H. A. et al. Y chromosome loss in cancer drives growth by evasion of adaptive immunity. *Nature* **619**, 624–631 (2023).

8. Qi, M., Pang, J., Mitsiades, I., Lane, A. A. & Rheinbay, E. Loss of chromosome Y in primary tumors. *Cell* https://doi.org/10.1016/j.cell.2023.06.006 (2023).
9. Rubin, J. B. et al. Sex differences in cancer mechanisms. *Biol. Sex Differ.* **11**, 17 (2020).
10. Wuidar, V. et al. Sex-based differences in the tumor microenvironment. *Adv. Exp. Med. Biol.* **1329**, 499–533 (2021).
11. Guan, X. et al. Androgen receptor activity in T cells limits checkpoint blockade efficacy. *Nature* **606**, 791–796 (2022).
12. Gittleman, H. et al. Sex is an important prognostic factor for glioblastoma but not for nonglioblastoma. *Neurooncol. Pract.* **6**, 451–462 (2019).
13. Sun, T. et al. Sexually dimorphic RB inactivation underlies mesenchymal glioblastoma prevalence in males. *J. Clin. Invest.* **124**, 4123–4133 (2014).
14. Yang, W. et al. Sex differences in GBM revealed by analysis of patient imaging, transcriptome, and survival data. *Sci. Transl. Med.* **11**, eaao5253 (2019).
15. Bayik, D. et al. Myeloid-derived suppressor cell subsets drive glioblastoma growth in a sex-specific manner. *Cancer Discov.* **10**, 1210–1225 (2020).
16. Lee, J. et al. Sex-biased T-cell exhaustion drives differential immune responses in glioblastoma. *Cancer Discov.* **13**, 2090–2105 (2023).
17. Turaga, S. M. et al. JAM-A functions as a female microglial tumor suppressor in glioblastoma. *Neuro. Oncol.* **22**, 1591–1601 (2020).
18. Rodriguez-Lozano, D. C., Pina-Medina, A. G., Hansberg-Pastor, V., Bello-Alvarez, C. & Camacho-Arroyo, I. Testosterone promotes glioblastoma cell proliferation, migration, and invasion through androgen receptor activation. *Front. Endocrinol.* **10**, 16 (2019).
19. Werner, C. K. et al. Expression of the androgen receptor governs radiation resistance in a subset of glioblastomas vulnerable to antiandrogen therapy. *Mol. Cancer Ther.* **19**, 2163–2174 (2020).
20. Zhao, N. et al. Androgen receptor, although not a specific marker for, is a novel target to suppress glioma stem cells as a therapeutic strategy for glioblastoma. *Front. Oncol.* **11**, 616625 (2021).
21. Hines, M., Constantinescu, M. & Spencer, D. Early androgen exposure and human gender development. *Biol. Sex Differ.* **6**, 3 (2015).
22. Sato, T. et al. Brain masculinization requires androgen receptor function. *Proc. Natl Acad. Sci. USA* **101**, 1673–1678 (2004).
23. Azcoitia, I., Mendez, P. & Garcia-Segura, L. M. Aromatase in the human brain. *Androg. Clin. Res. Ther.* **2**, 189–202 (2021).
24. Immenschuh, J. et al. Sex differences in distribution and identity of aromatase gene expressing cells in the young adult rat brain. *Biol. Sex Differ.* **14**, 54 (2023).
25. Hu, L. S. et al. Integrated molecular and multiparametric MRI mapping of high-grade glioma identifies regional biologic signatures. *Nat. Commun.* **14**, 6066 (2023).
26. Fane, M. & Weeraratna, A. T. How the ageing microenvironment influences tumour progression. *Nat. Rev. Cancer* **20**, 89–106 (2020).
27. Feldman, H. A. et al. Age trends in the level of serum testosterone and other hormones in middle-aged men: longitudinal results from the Massachusetts male aging study. *J. Clin. Endocrinol. Metab.* **87**, 589–598 (2002).
28. Zhang, X. et al. Androgen signaling contributes to sex differences in cancer by inhibiting NF-κB activation in t cells and suppressing antitumor immunity. *Cancer Res.* **83**, 906–921 (2023).
29. Garcia-Diaz, C. et al. Glioblastoma cell fate is differentially regulated by the microenvironments of the tumor bulk and infiltrative margin. *Cell Rep.* **42**, 112472 (2023).
30. Clements, M., Simpson Ragdale, H., Garcia-Diaz, C. & Parrinello, S. Generation of immunocompetent somatic glioblastoma mouse models through in situ transformation of subventricular zone neural stem cells. *STAR Protoc.* **5**, 102928 (2024).
31. Dai, C., Dehm, S. M. & Sharifi, N. Targeting the androgen signaling axis in prostate cancer. *J. Clin. Oncol.* **41**, 4267–4278 (2023).
32. Acharya, N. et al. Endogenous glucocorticoid signaling regulates $CD8^+$ T cell differentiation and development of dysfunction in the tumor microenvironment. *Immunity* **53**, 658–671 (2020).
33. Alyamani, M. et al. Deep androgen receptor suppression in prostate cancer exploits sexually dimorphic renal expression for systemic glucocorticoid exposure. *Ann. Oncol.* **31**, 369–376 (2020).
34. Bellavance, M. A. & Rivest, S. The HPA–immune axis and the immunomodulatory actions of glucocorticoids in the brain. *Front. Immunol.* **5**, 136 (2014).
35. Tuckermann, J. P. et al. Macrophages and neutrophils are the targets for immune suppression by glucocorticoids in contact allergy. *J. Clin. Invest.* **117**, 1381–1390 (2007).
36. Varga, G. et al. Glucocorticoids induce an activated, anti-inflammatory monocyte subset in mice that resembles myeloid-derived suppressor cells. *J. Leukoc. Biol.* **84**, 644–650 (2008).
37. Jarmula, J. et al. Macrophage migration inhibitory factor as a therapeutic target in neuro-oncology: a review. *Neurooncol. Adv.* **6**, vdae142 (2024).
38. Ruiz-Moreno, C. et al. Charting the single-cell and spatial landscape of IDH-wild-type glioblastoma with GBmap. *Neuro. Oncol.* **27**, 2281–2295 (2025).
39. Konsman, J. P. in *Neuroendocrine–Immune System Interactions* (eds Konsman J. P. & Reyes T. M.) 91–104 (Springer, 2023).
40. Miller, T. E. et al. Programs, origins and immunomodulatory functions of myeloid cells in glioma. *Nature* **640**, 1072–1082 (2025).
41. Singh, J., Habean, M. L. & Panicker, N. Inflammasome assembly in neurodegenerative diseases. *Trends Neurosci.* **46**, 814–831 (2023).
42. Jang, G. Y. et al. Interactions between tumor-derived proteins and Toll-like receptors. *Exp. Mol. Med.* **52**, 1926–1935 (2020).
43. Rathkey, J. K. et al. Chemical disruption of the pyroptotic pore-forming protein gasdermin D inhibits inflammatory cell death and sepsis. *Sci. Immunol.* **3**, eaat2738 (2018).
44. Panicker, N. et al. Fyn kinase regulates misfolded α-synuclein uptake and NLRP3 inflammasome activation in microglia. *J. Exp. Med.* **216**, 1411–1430 (2019).
45. O'Keefe, M. E., Kondolf, H. C., De Santis, S., Pizarro, T. T. & Abbott, D. W. Restraint of inflammasome-driven cytokine responses through the mRNA stability protein TTP. *Cell Rep.* **44**, 115340 (2025).
46. Liu, Y., Zhou, F., Ali, H., Lathia, J. D. & Chen, P. Immunotherapy for glioblastoma: current state, challenges, and future perspectives. *Cell. Mol. Immunol.* **21**, 1354–1375 (2024).
47. Gonzalez-Aponte, M. F. et al. Daily glucocorticoids promote glioblastoma growth and circadian synchrony to the host. *Cancer Cell* **43**, 144–160 (2025).
48. Ostrom, Q. T. et al. CBTRUS statistical report: primary brain and other central nervous system tumors diagnosed in the United States in 2013–2017. *Neuro. Oncol.* **22**, iv1–iv96 (2020).
49. Kim, M. et al. Glioblastoma as an age-related neurological disorder in adults. *Neurooncol. Adv.* **3**, vdab125 (2021).
50. Chitnis, T. The role of testosterone in MS risk and course. *Mult. Scler.* **24**, 36–41 (2018).
51. Kostaras, X., Cusano, F., Kline, G. A., Roa, W. & Easaw, J. Use of dexamethasone in patients with high-grade glioma: a clinical practice guideline. *Curr. Oncol.* **21**, e493–e503 (2014).

Methods

Cell lines

The syngeneic mouse GBM model SB28 was provided by H. Okada, and GL261 was obtained from the Developmental Therapeutic Program, NCI. CPA was provided by the Castro-Lowenstein Laboratory, and KR158 was provided by L. Deleyrolle. The mouse bladder cancer cell line MB49 was obtained from the Animal Tumour Core at the Cleveland Clinic. The mouse melanoma B16-F10 cells were a gift from T. Stappenbeck. The GBM patient-derived xenograft cell model L1 was obtained from B. Reynolds (originally from the laboratory of A. Vescovi) and GBM23 was obtained from E. Sulman.

After thawing, all cell lines were treated with 1:100 MycoRemoval agent (MP Biomedicals) and regularly tested for *Mycoplasma* spp. (Lonza). GBM cell lines were maintained in complete RPMI 1640 (Media Preparation Core, Cleveland Clinic) supplemented with 10% FBS (Thermo Fisher), 1% penicillin–streptomycin (Media Preparation Core) and GlutaMAX (Gibco). MB49 and B16-F10 cells were cultured in DMEM (Media Preparation Core, Cleveland Clinic) supplemented with 10% FBS, 1% penicillin–streptomycin, GlutaMAX and sodium pyruvate (Thermo Fisher Scientific). GBM patient-derived xenograft cells were cultured in DMEM/F12 medium (ThermoFisher) supplemented with 1% penicillin–streptomycin (ThermoFisher Scientific), 1% B27 without vitamin A (ThermoFisher), 20 ng ml^{-1} EGF (R&D Systems) and 20 ng ml^{-1} FGF (R&D Systems). Cells were cultured in humidified incubators at 37 °C and 5% CO_2 and were not allowed to exceed 15 passages.

Mice

All animals were kept in a specific pathogen-free facility of the Biological Resource Unit at the Lerner Research Institute, Cleveland Clinic, with a 12-h light–dark cycle. All animal procedures were performed in accordance with the guidelines and protocols approved by the Institutional Animal Care and Use Committee at the Cleveland Clinic. All mouse strains used in the study are listed in Supplementary Table 7.

Castration

Two weeks before tumour implantation, 5–6-week-old male mice underwent either castration or sham surgery. Mice were maintained under inhalation anaesthesia (2–2.5% isoflurane) through a nose cone and administered an ophthalmic lubricant to prevent corneal dryness. The scrotal area was disinfected using betadine and alcohol. A small horizontal incision was made in the skin of the scrotum and the inner skin membranes, and the testicles were exteriorized. Using resorbable vicryl sutures, testicular arteries were ligated, followed by the removal of testicles. The incision was closed using surgical clips (Fine Science Tools). For pain control, subcutaneous injections of buprenorphine (0.1 mg kg^{-1}) and bupivacaine (5 mg kg^{-1}) were administered. In sham-surgery mice, the same procedure was performed, excluding the ligation and removal of the testis.

Microglia depletion

Two weeks after castration, mice were fed either a control diet (AIN-76A) or a PLX3397-supplemented diet (660 mg kg^{-1}; Research Diets) ad libitum. Mice then received intracranial tumour cell injections and remained on the assigned diet until the experimental end point.

Tumour implantation and treatments

For intracranial tumour implantation, mice were anaesthetized by inhalation anaesthesia (2–2.5% isoflurane), secured in a stereotaxis apparatus and intracranially injected with tumour cells suspended in 5 µl RPMI-null medium with the following numbers: SB28, 10,000–15,000 cells per mouse; GL261, 20,000–25,000 cells per mouse; CPA, 10,000 cells per mouse; KR158, 50,000 cells per mouse; MB49, 5,000 cells per mouse; and B16-F10, 40,000 cells per mouse. Tumour injections were targeted to the left hemisphere approximately 0.5 mm rostral and 1.8 mm lateral to the bregma with a depth of 3.5 mm from the scalp, which does not directly contact or lie near the hypothalamus. The needle was held in place an additional 60 s before slow and measured removal. The animals were monitored to detect the onset of neurological and behavioural symptoms indicative of the presence of a brain tumour.

For the GEMM, we used CRISPR-mediated somatic gene deletion using a previously described in vivo electroporation approach[30]. In brief, plasmids carrying Cas9 and CRISPR guide RNAs targeting *Nf1*, *Pten* and *Trp53* were injected into the lateral ventricle of postnatal day 2 mouse pups, followed immediately by electroporation to enable plasmid uptake into neural stem cells. Mice were weaned at postnatal day 21, and only male mice were used in the study.

For subcutaneous tumour implantation, mice were anaesthetized by inhalation anaesthesia (2–2.5% isoflurane). A total of 500,000 SB28 cells were suspended in 100 µl RPMI-null medium and subcutaneously injected into the right flank of the mouse. Tumour size was measured starting from day 10, when the tumour becomes palpable, and measurements were taken every 2 days.

In some experiments, gonadally intact 5–6-week-old male or female mice received intraperitoneal injections of enzalutamide (10 mg kg^{-1}; SellekChem) or vehicle (corn oil) beginning 2 days before tumour implantation. The injections were repeated every 2–3 days until the experimental end point was reached. In other experiments, intraperitoneal injections of mifepristone (25 mg kg^{-1}; Cayman Chemical) or vehicle (corn oil) were initiated 2 days before tumour implantation and were repeated every 2–3 days until reaching the end point.

To restore testosterone levels in castrated male mice or female mice, testosterone cypionate injections (12.5 mg kg^{-1}; Hikma Pharmaceuticals) were given subcutaneously 1 week before tumour implantation and repeated once a week.

GBM cell lysates were prepared by sonicating SB28 cells for 30 min followed by a freeze–thaw cycle. The concentration of the tumour cell suspension used for lysate preparation matched that used for tumour implantation. For the latex beads experiment, FluoSpheres polystyrene microspheres (15 µm; Invitrogen) were intracranially implanted (10,000 beads per mouse).

To inhibit cytokine signalling, mice were intraperitoneally injected with 200 µg anti-IL-1β, anti-TNF antibody or isotype antibody (BioXcell) on day −1 and day 0 of tumour implantation and injections were repeated every 2–3 days until the experimental end point.

Tumour and tissue dissociation for flow cytometry

At the indicated time points, mice were euthanized and brain tumour, spleen and lymph nodes (inguinal) were collected. Brain tumour tissue was minced into small pieces with scalpels and subjected to enzymatic digestion in the presence of collagenase D (1 mg ml^{-1}; Roche) and DNase I (0.1 mg ml^{-1}; Roche) at 37 °C. Digested tissue was filtered through a 70 µm cell strainer. To enrich immune cells, gradient centrifugation was performed using 30% Percoll solution (Sigma). Red blood cells (RBCs) were lysed using RBC lysis buffer (BioLegend). For spleen and lymph nodes, tissue was ground onto a 40 µm cell strainer, followed by RBC lysis. All single-cell suspension samples were filtered once more with a 40 µm cell strainer before staining for flow cytometry.

Flow cytometry

Cells were stained with the antibodies listed in Supplementary Table 8. In brief, after live/dead staining with LIVEDEAD Blue (Thermo Fisher Scientific) on ice for 15 min, cells were washed and incubated with FcR blocker (Miltenyi Biotech) diluted in PBS and 2% BSA on ice for 10 min. For surface staining, cells were incubated in an antibody mixture diluted in brilliant buffer (BD Biosciences) at 1:100 to 1:250 on ice for 30 min. After washing with PBS and 2% BSA buffer, cells were fixed with FOXP3/transcription factor fixation buffer (eBioscience) at 4 °C overnight. For intracellular staining, antibodies were diluted in FOXP3/transcription factor permeabilization buffer at a ratio of 1:250, and cells were incubated at room temperature for 45 min. For intracellular cytokine detection, cells were stimulated using Cell Stimulation Cocktail plus protein transport inhibitor (eBioscience) in complete RPMI for 4 h, followed by the cell-staining procedures described above. Stained cells were acquired using a Cytek Aurora instrument with SpectroFlow software (v.3.3.0, Cytek Biosciences) or a BD Fortessa instrument with FACSDiva software (v.9.0, BD Biosciences) and analysed using FlowJo software (v.10, BD Biosciences) following a previously published gating strategy[16] (shown in Extended Data Fig. 4b). t-SNE analysis was performed using FlowJo software.

Image-localized biopsy deconvolution and analysis

A total of 202 biopsy samples collected from 58 patients (22 women, 36 men) with high-grade glioma were analysed for bulk RNA-seq[25,52]. Using CIBERSORTx[53] and a scRNA-seq reference dataset of the glioma microenvironment with clustered cell states, including T cells[54], deconvolution of bulk RNA-seq data was performed to produce estimates of T cell abundances in each sample. Owing to the limited storage available on the CIBERSORTx online interface, snRNA was downsampled 3 times to produce 100 of each cell state as input into the algorithm, each run 6 times. We present an average across runs. Statistics presented for this dataset are a result of *t*-test within patient sex. T cell values were averaged within patients not to violate the assumption of independent samples.

Phosphorylation array

Hypothalamic tissue samples were isolated from castrated mice and sham-surgery mice 14 days after tumour implantation. Proteins were extracted following the manufacturer's instructions and phosphorylation events were analysed using a Phospho Explorer Antibody array (Full Moon Biosystems), with array scanning and quantification performed by the service provider. Phosphorylation signals with a fold change greater than 1.3 or less than 0.7 were considered for further analyses. Canonical pathway analysis and upstream regulator prediction were conducted using Ingenuity Pathway Analysis (Qiagen).

Immunofluorescence staining and image analysis

For immunofluorescence analysis, animals underwent high-pressure transcardiac perfusion with 4% formalin. Brains were post-fixed in the calvarium for an additional 24 h before careful dissection and sequential dehydration, first in 30% sucrose then in a 1:1 solution of 60% sucrose and optimal cutting temperature (OCT) compound. Cryoprotected brains were embedded in OCT compound, and 30 µm fixed-frozen sections were prepared using a Leica CM1950 cryostat. For staining, tissue sections were blocked overnight at 4 °C in a PBS-based blocking solution of 5% normal donkey serum, 1 mg ml^{-1} bovine serum albumin and 0.3% Triton X-100. Primary and secondary antibodies were bound during sequential overnight incubations at 4 °C in blocking solution. Nuclei were counterstained using Hoechst 33342 dissolved in PBS with 0.1% Triton X-100. The following primary antibodies were used at 1:1,000 dilution: chicken anti-GFP (Aves Labs), rabbit anti-cleaved caspase-3 (Cell Signaling), rabbit anti-phospho-histone H3 (Cell Signaling), rabbit anti-c-FOS (EnCor Biotechnology), goat anti-IBA1 (Abcam) and rabbit anti-ASC (Adipogen). Donkey or rabbit raised secondary antibodies were used that were conjugated to Alexa Fluor 488, 555 or 647 fluorescent dyes. To visualize cell death with cleaved caspase-3, tissue sections underwent heat-induced epitope retrieval in 10 mM citrate buffer with 0.5% Tween 20 for 45 min at 95 °C before the first blocking step. Stained tissue was digitized at ×10 magnification using an Akoya Biosciences PhenoImager HT. Digital fluorescent micrographs were analysed using the Positive Cell Detection Pipeline in QuPath[55]. Fluorescent images were acquired using a Leica Stellaris5 confocal microscope. IMARIS software (Oxford Instruments) was used to prepare 3D reconstructions of the images.

Tissue mRNA extraction and RT–qPCR

At the indicated time points, brain tissue was collected and flash-frozen and stored at −80 °C until processing. Total RNA was isolated using QIAzol Lysis reagent (Qiagen) following the standard protocol, including tissue homogenization. cDNA was synthesized using a High-capacity cDNA Reverse Transcription kit (Applied Biosystems). qPCR reactions were performed using TaqMan probes and Fast Advanced mater mix (Applied Biosystems) on an Applied Biosystems QuantStudio 5Real-Time PCR system. The threshold cycle (C_t) value for each gene was normalized to the expression levels of *Gapdh*, and relative expression was calculated by normalizing to the average delta C_t value of the control group.

In vitro tumour cell proliferation assessment

Tumour cell proliferation was monitored and quantified using an IncuCyte Live-Cell Analysis system. For these experiments, 4 technical replicates of SB28 (500 cells per well, 200 µl) and GL261 (1,000 cells per well, 200 µl) cells were plated in flat-bottom 96-well plates and treated with testosterone cypionate or vehicle (corn oil, 2 µl per well). Data were captured for up to 120 h of incubation.

ELISA

Serum was collected at the indicated time points or at the neurological end point. ACTH levels were measured using a mouse/rat ACTH ELISA kit (Abcam) following the manufacturer's instructions. Serum was diluted at a ratio of 1:2 to 1:4. Serum testosterone levels were measured using a Testosterone ELISA kit (Cayman chemical) according to the manufacturer's protocol. Plates were read at 600 nm or 450 nm using a Victor Nivo (Perkin Elmer) multimode plate reader.

Immunoblotting

Brain tissue samples were collected and flash-frozen using liquid nitrogen and kept in −80 °C until use. Tissue protein lysates were prepared as previously described[56]. In brief, tissue samples were homogenized in RIPA buffer using a motorized hand-held pestle. Lysates were then subjected to 3 freeze–thaw cycles and spun down at 13,000*g* for 45 min. The protein content of the isolated supernatants was quantified using a BCA kit (Pierce). A total of 20–25 µg protein lysate was loaded onto 4–20% Tris Glycine gels (Thermo Fisher) and proteins were transferred to nitrocellulose membranes. After blocking with Intercept Blocking buffer (LiCor Biosciences), membranes were incubated with primary mouse anti-caspase-1 antibody (1:1,000; Adipogen), followed by IR-680-conjugated anti-mouse secondary antibody (1:10,000; LiCor Bio). Fluorescent western blots were imaged using a LiCor Odyssey CLx system (LiCor Biosciences). Membranes were re-probed with β-actin antibody (1:10,000; Sigma-Aldrich) and β-actin bands were visualized by enhanced chemiluminescence (Thermo Scientific). Unprocessed immunoblot images are provided in Supplementary Fig. 5.

In vitro treatment of macrophages overexpressing ASC-mCerulean

Immortalized macrophages overexpressing ASC-mCerulean[57] were provided by D. Abbott. Cells were cultured in DMEM supplemented with 10% charcoal-stripped FBS (Gibco) to avoid residual hormone effects and 1% penicillin–streptomycin (Media Preparation Core) and maintained in 5 µg ml^{-1} puromycin until use. To assess the effect of androgen signalling, cells were plated onto glass coverslips and incubated with either dihydrotestosterone (DHT; Sigma-Aldrich) or vehicle control (methanol) for 72 h. After washing, cells were stimulated with LPS (500 ng ml^{-1}; Sigma) or GBM lysates (SB28) for 4 h. Nigericin (10 nM; Sigma) was then added during the final 45 min of stimulation. After stimulation, 2.5 µM DRAQ5 (Life Technologies) was added to the cells for 30 min. Cells were then fixed with 4% paraformaldehyde for 20 min and washed with PBS 3 times. Coverslips were mounted onto slides using Aqua-Mount (Epredia). For confocal microscopy analysis, fluorescent images were acquired using a Leica Stellaris5 confocal microscope. To assess the percentage of ASC-speck-positive cells, the number of speck-positive cells for each image was divided by the number of DRAQ5-positive cells. The mCerulean signal intensity via flow cytometry was also measured using BDSymphony. Supernatants were collected, and secreted IL-1β levels were quantified by ELISA (Abcam).

MS analysis

Freshly collected mouse serum samples were stored at −80 °C until analysis. Concentrations of glucocorticoids and testosterone were measured by LC–MS/MS as previously described[58]. In brief, 60 µl thawed serum was spiked with an internal standard mix (androstene-3,17-dione-2,3,4-$^{13}C_3$, 5α-dihydrotestosterone-16,17,17-D_3 and cortisol-9,11,12,12-D_4). Protein precipitation was followed by adding acetonitrile, and the supernatant was collected to extract glucocorticoids and testosterone using methyl-tert-butyl ether through a liquid–liquid extraction procedure. The steroid fraction was collected, dried and reconstituted in 140 µl of 50% methanol. The reconstituted sample underwent LC–MS/MS analysis on a Shimadzu UPLC system with a C18 column (Zorbax Eclipse Plus C_{18} column, 150 mm × 2.1 mm, 3.5 µm, Agilent) coupled to a QTrap 5500 mass spectrometer (AB Sciex). Data acquisition and processing were performed using MultiQuant (AB Sciex; v.0.3).

Bulk RNA-seq

For tumour cell sequencing, tumour tissue samples were collected from castrated mice and sham-surgery mice 14 days after intracranial implantation of GBM cells (SB28, 15,000 cells per mouse). For hypothalamus sequencing, hypothalamus tissue samples were collected from castrated mice and sham-surgery mice 14 days after intracranial implantation of SB28 or injection with medium. Total RNA was isolated using a Maxwell RSC simplyRNA Tissue kit, and RNA quality and quantity were measured using a Tapestation 4200 (Agilent Technologies) and a Qubit Flex Fluorometer (Invitrogen), respectively. Libraries were generated using an Illumina TruSeq Stranded mRNA kit following the manufacturer's protocol with 300 ng RNA as input. The process involved poly-A-containing mRNA purification using poly-T oligonucleotide-attached magnetic beads, followed by fragmentation of the mRNA into small pieces using divalent cations under elevated temperature. First-strand cDNA synthesis was performed using reverse transcriptase and random primers, with actinomycin D included to improve strand specificity. Second-strand cDNA synthesis was achieved using DNA polymerase I and RNase H, replacing dTTP with dUTP in the mix to ensure strand specificity. The 3′ ends of the cDNA fragments were adenylated to prevent self-ligation, and adapters were ligated to prepare the cDNA for hybridization onto a flow cell. The cDNA libraries were enriched by PCR and purified. Libraries were quantified using a Qubit Flex Fluorometer and their size distribution was assessed using a Tapestation 4200 (Agilent Technologies). Samples were sequenced on an Illumina NovaSeq 6000 for 200 cycles according to the manufacturer's recommendations for a depth of 20 million paired (40 million total) reads per library.

scRNA-seq

For scRNA-seq, samples were prepared 14 days after intracranial implantation of GBM cells (SB28, 15,000 cells per mouse). Single-cell suspensions were prepared from tumour and spleen samples obtained from castrated mice and sham-surgery mice as described above, and $CD45^+$ immune cells were sorted using a BigFoot Spectral Cell Sorter (ThermoFisher). The scRNA-seq libraries were prepared from the sorted immune cells following the manufacturer's Chromium Single Cell 3′ protocol (10x Genomics). In brief, we targeted 10,000 single cells using the 10x Genomics Chromium Controller for cDNA synthesis and barcoding, followed by evaluation of the quality and quantity of cDNA in each sample using a Bioanalyzer High Sensitivity DNA assay. The cDNA was used as the initial material for the subsequent steps, including fragmentation, end repair, adapter ligation and sample indexing. To ensure the proper construction of sample libraries, the same Bioanalyzer assay was used. Once constructed, the libraries were pooled and quantified using a Quantabio Q cycler. They were then denatured and sequenced on an Illumina Novaseq 6000 high-throughput sequencing platform. The sequencing protocol included 28 cycles for the forward read and 91 cycles for the reverse read.

Bioinformatic analysis of bulk RNA-seq and scRNA-seq data

Bulk transcriptomic FASTQ data quality was assessed using FastQC (v.0.11.8)[59]. Reads were aligned to the GRCm38 (mm10) mouse reference genome using STAR (v.2.7.3a)[60]. Expression quantification of the transcripts was done using Salmon (v.0.14.1)[61] with the GRCm38 (mm10) mouse reference genome. Gene-level expression quantification was calculated using tximeta (v.1.24.0)[62] in R (v.4.4.1) with the Ensembl GRCm38 release 98 GTF file. Differential expression analyses between castrated mice and sham-surgery mice were performed using DESeq2 (v.1.46.0)[63]. Volcano plots of DEGs were generated using EnhancedVolcano (v.1.24.0)[64]. Statistically overrepresented GO terms and pathways were identified using clusterProfiler (v.4.14.6)[65] and the PANTHER database[66].

scRNA-seq data of CD45-sorted immune cells were mapped to the mouse reference mm10 (v.1.2.0) using 10x Genomics Cell Range (v.7.2.0). Filtered feature matrices were loaded to Seurat (v.5.2.1)[67]. Sample batch effects were controlled during the integration process using the reciprocal PCA method with pairwise anchoring in Seurat. Integrated data were clustered using the Leiden clustering algorithm[68] at a resolution of 0.6. The Leiden method was implemented using the Python module leidenalg (v.0.10.2) in Python (v.3.12.8), which was loaded with reticulate (v.1.40.0) into R. After clustering, immune-cell-type classification was done using ScType (v.1.0)[69] with the 'Immune system' tissue selection. For each cell type, differential expression analysis after pseudobulking was performed in Seurat with the DESeq2 method. Immune cell–cell communications were estimated using CellChat (v.2.1.2)[70]. Subsequently, T cell populations in the brain and macrophage populations in the spleen were selected, and we performed subclustering to identify finer cell population compositions. GSEA was performed using clusterProfiler (v.4.14.6) with genome-wide annotation for mouse org.Mm.eg.db (v.3.20.0) and the Molecular Signatures Database[71] R implementation msigdbr (v.10.0.1)[72].

Spatial transcriptomics

For digital spatial profiling, mice were subjected to cardiac perfusion with a solution of 4% formaldehyde in PBS. The brain was post-fixed in the calvarium for an additional 16–24 h before the intact brain was isolated into a solution of 70% ethanol. Preserved brain specimens were dehydrated with ascending concentrations of ethanol, cleared with xylene and embedded in paraffin. Formalin-fixed paraffin-embedded mouse brain samples were sectioned onto four slides for GeoMx digital spatial profiling slide processing. Each slide contained sections from three biological replicates for each time point per condition. All slides were processed for GeoMx Mouse Whole Transcriptome Atlas (MuWTA) collections according to Nanostring protocols. Slides were baked for 18 h at 60 °C before deparaffinization to increase tissue adhesion. After deparaffinization, slides underwent target retrieval in 1× Tris-EDTA at 99 °C for 20 min, followed by protease K digestion at a concentration of 1 µg ml^{-1} for 15 min and post-fixation with 10% NBF. MuWTA probes were added and hybridized overnight at 37 °C. The next day, slide preparation continued with stringent washes, blocking with Nanosting Buffer W and then staining with pre-conjugated antibodies. For this assay, the slides were stained with Syto13 (1:10; Nanostring), CD45 (1:40; Nanostring, AF594 conjugate) and IBA1 (1:100; Cell Signaling Technologies, AF647 conjugate). The slides were scanned on a

GeoMx instrument (v.3.1.2.12), and ROIs were placed on each slide in cortical, hypothalamus and intratumoral regions in each replicate. Each ROI was divided into IBA1$^+$ and IBA1$^-$ cell segments by thresholding on the basis of IBA1 antibody fluorescence. For each unique segment, the barcoded MuWTA probes were collected into a 96-well plate. The collected segment probes were amplified by PCR, pooled based on their corresponding segment area and sequenced on an Illumina NovaSeq X Plus platform. Fastq files were converted into digital count conversion files using the GeoMx NGS pipeline (v.3.1.3.6) and uploaded to the GeoMx Analysis suite (v.3.1.2.12) for data analysis.

Raw count data were normalized using the DESeq2 variance-stabilized transformation function. Negative control probes were used to establish a variance threshold, which was defined as the mean plus two standard deviations of the negative probe variance. Only genes exceeding this threshold were retained for downstream analyses. Differential gene expression analysis was performed using the limma package. Linear models were fitted to normalized expression data using the lmFit function followed by empirical Bayes moderation with eBayes. The design matrices incorporated treatment effects while controlling relevant covariates including spatial regions and time point (Supplementary Table 6). GSEA was performed using the fgsea package with pre-ranked gene lists from the MsigDBR package, including Hallmark, KEGG, Reactome, WIKIPATHWAYS and a customized set of ontologies found from the literature. Results were visualized using GGplot2. Cell signatures were taken from previous publications[38,40] and used to score GeoMx samples for each signature and visualized using Complexheatmap. No multiple testing correction was applied to individual gene *P* values in the limma analysis, but pathway-level statistics were adjusted for multiple testing using the Benjamini–Hochberg method. R (v.4.4.1) was used for all analyses.

Real-world data analysis

Real-world data were obtained from linked SEER data and Medicare claims for male patients with GBM diagnosed from 1 January 2008 to 31 December 2019 with corresponding Medicare claims and follow up for survival until 31 December 2021. The standard-of-care therapy for GBM is maximum surgical resection and concomitant chemoradiation[73,74]. Therefore, the analysis was limited to individuals who received surgical resection (categorized as biopsy only, subtotal resection, gross total resection and surgery not otherwise specified), radiation and temozolomide, which led to 1,333 cases for analysis. Survival was assessed in individuals receiving temozolomide only compared with those who received both temozolomide and supplementary testosterone using Cox proportional hazard models adjusted for demographics, extent of resection and Charlson comorbidity scores to estimate HR, 95% CI and *P* values. Significance was assessed at an alpha level 0.05 for the *P* values. Additional details are provided in the Supplementary Information.

Statistical analysis

GraphPad Prism (v.9, GraphPad Software) software was used for data presentation and statistical analyses. Unpaired two-sided *t*-test or one-way or two-way ANOVA was used with Tukey's multiple comparisons test, as indicated in the figure legends. Survival analysis was performed using log-rank tests. $P < 0.05$ was considered significant.

Reporting summary

Further information on research design is available in the Nature Portfolio Reporting Summary linked to this article.

Data availability

The bulk RNA-seq, scRNA-seq data and spatial transcriptomic data have been deposited, with the following links, into BioProject in the NCBI BioProject database: PRJNA1254286 (RNA-seq of tumours), PRJNA1254297 (RNA-seq of hypothalamus samples), PRJNA1254695 (scRNA-seq of immune cells) and PRJNA1372687 (spatial transcriptomics). For image-localized biopsy data analyses, data are publicly available online (https://www.synapse.org/#!Synapse:syn52256644). Mouse reads were aligned to the GRCm38 (mm10) mouse reference genome and human reads were aligned to the GRCh37 human reference genome. All data generated in this study are available upon request from the corresponding author. Source data are provided with this paper.

52. Bond, K. M. et al. Glioblastoma states are defined by cohabitating cellular populations with progression-, imaging- and sex-distinct patterns. Preprint at *bioRxiv* https://doi.org/10.1101/2022.03.23.485500 (2022).
53. Newman, A. M. et al. Determining cell type abundance and expression from bulk tissues with digital cytometry. *Nat. Biotechnol.* **37**, 773–782 (2019).
54. Al-Dalahmah, O. et al. Re-convolving the compositional landscape of primary and recurrent glioblastoma reveals prognostic and targetable tissue states. *Nat. Commun.* **14**, 2586 (2023).
55. Bankhead, P. et al. QuPath: Open source software for digital pathology image analysis. *Sci. Rep.* **7**, 16878 (2017).
56. Panicker, N. et al. Neuronal NLRP3 is a parkin substrate that drives neurodegeneration in Parkinson's disease. *Neuron* **110**, 2422–2437 (2022).
57. Stutz, A., Horvath, G. L., Monks, B. G. & Latz, E. in *The Inflammasome: Methods and Protocols* (eds De Nardo, C. M. & Latz, E.) 91–101 (Humana Press, 2013).
58. Zhu, Z. et al. Loss of dihydrotestosterone-inactivation activity promotes prostate cancer castration resistance detectable by functional imaging. *J. Biol. Chem.* **293**, 17829–17837 (2018).
59. Andrews, S. FastQC: a quality control tool for high throughput sequence data. *Babraham Bioinformatics* http://www.bioinformatics.babraham.ac.uk/projects/fastqc/ (2010).
60. Dobin, A. et al. STAR: ultrafast universal RNA-seq aligner. *Bioinformatics* **29**, 15–21 (2013).
61. Patro, R., Duggal, G., Love, M. I., Irizarry, R. A. & Kingsford, C. Salmon provides fast and bias-aware quantification of transcript expression. *Nat. Methods* **14**, 417–419 (2017).
62. Love, M. I. et al. Tximeta: reference sequence checksums for provenance identification in RNA-seq. *PLoS Comput. Biol.* **16**, e1007664 (2020).
63. Love, M. I., Huber, W. & Anders, S. Moderated estimation of fold change and dispersion for RNA-seq data with DESeq2. *Genome Biol.* **15**, 550 (2014).
64. Blighe K., Rana S., Lewis M. EnhancedVolcano: publication-ready volcano plots with enhanced colouring and labeling. R version 1.24.0. *GitHub* https://github.com/kevinblighe/EnhancedVolcano (2024).
65. Yu, G., Wang, L. G., Han, Y. & He, Q. Y. clusterProfiler: an R package for comparing biological themes among gene clusters. *Omics* **16**, 284–287 (2012).
66. Thomas, P. D. et al. PANTHER: making genome-scale phylogenetics accessible to all. *Protein Sci.* **31**, 8–22 (2022).
67. Hao, Y. et al. Dictionary learning for integrative, multimodal and scalable single-cell analysis. *Nat. Biotechnol.* **42**, 293–304 (2024).
68. Traag, V. A., Waltman, L. & van Eck, N. J. From Louvain to Leiden: guaranteeing well-connected communities. *Sci. Rep.* **9**, 5233 (2019).
69. Ianevski, A., Giri, A. K. & Aittokallio, T. SynergyFinder 3.0: an interactive analysis and consensus interpretation of multi-drug synergies across multiple samples. *Nucleic Acids Res.* **50**, W739–W743 (2022).
70. Jin, S. et al. Inference and analysis of cell–cell communication using CellChat. *Nat. Commun.* **12**, 1088 (2021).
71. Liberzon, A. et al. Molecular signatures database (MSigDB) 3.0. *Bioinformatics* **27**, 1739–1740 (2011).
72. Dolgalev, I. msigdbr: MSigDB gene sets for multiple organisms in a Tidy Data format. R version 10.0.1. *GitHub* https://github.com/igordot/msigdbr (2025).
73. Stupp, R. et al. Radiotherapy plus concomitant and adjuvant temozolomide for glioblastoma. *N. Engl. J. Med.* **352**, 987–996 (2005).
74. Wen, P. Y. et al. RANO 2.0: update to the response assessment in neuro-oncology criteria for high- and low-grade gliomas in adults. *J. Clin. Oncol.* **41**, 5187–5199 (2023).

Acknowledgements We thank the members of the Lathia laboratory for insightful and constructive discussions; E. Mulkearns-Hubert for editorial assistance; A. Mendelsohn for her illustrative work in Fig. 1f,h and Supplementary Fig. 4; R. Fairchild for commenting on the manuscript; R. Khatib for his inspiration and support of our work; staff at the Cleveland Clinic Flow Cytometry Core and Genomics Core for technical support; and staff at the National Cancer Institute, Information Management Services (IMS) and the SEER Program tumour registries for their creation of the SEER-Medicare database. This study used the linked SEER-Medicare database. The interpretation and reporting of these data are the sole responsibility of the authors. The collection of cancer incidence data used in this study was supported by the California Department of Public Health pursuant to California Health and Safety Code Section 103885; Centers for Disease Control and Prevention's (CDC) National Program of Cancer Registries, under cooperative agreement 1NU58DP007156; the National Cancer Institute's SEER Program under contract HHSN261201800032I awarded to the University of California, San Francisco, contract HHSN261201800015I awarded to the University of Southern California, and contract HHSN261201800009I awarded to the Public Health Institute. The ideas and opinions expressed herein are those of the author(s) and do not necessarily reflect the opinions of the State of California, Department of Public Health, the National Cancer Institute, and the Centers for Disease Control and Prevention or their Contractors and Subcontractors. This work was supported by NIH grants R35 NS127083 (to J.D.L.), P01 CA245705 (to J.D.L., J.B.R. and M.B.), F31 CA264849 (to K.E.K.), R01CA261995 (to N.S.), R01CA236780 (to N.S.), R01CA172382 (to N.S.), R00AG066862 (to N.P.), R35GM162199 (to N.P.), U54CA274504 (to K.R.S), U01CA250481 (to K.R.S) and U01CA220378 (to K.R.S). This work was also supported by the American Brain Tumor Association (to J.D.L., J.L., D.J.S. and J.J.), the Case Comprehensive

Cancer Center (to J.D.L.) and the Cleveland Clinic (to J.D.L., J.L., M.N. and A.A.-V.), as well as Ramon Areces Foundation postdoctoral grants (to A.A.-V.). This project was also supported with funding from the Preston Robert Tisch Brain Tumor Center, the Duke Cancer Institute (P30CA014236) (to Q.T.O.), and pilot funding from the Duke Center for Brain and Spine Metastasis (to Q.T.O.). This work was also supported by American Cancer Society AZ Discovery Boost Award (to K.R.S.). The work of N.P. was supported by the National Institute of Aging (P30 AG072959 grant) as a REC Scholar of the Cleveland Alzheimer's Disease Research Center (CADRC).

Author contributions J.L., M.N. and J.D.L. conceptualized and designed the experiments. J.L., Y.H., D.S.L.H., L.C. and M.N. developed the methodology. J.L., Y.-M.C., D.J.S., Y.H., A.E., A.M.S., L.C., J.R.B., C.A.P.B., K.L., A.A.-V., J.G., C.L., S.K., R.N., J.V., E.S.H., R.F., J.J., S.Z.W. and K.E.K. conducted experiments and acquired data. J.L., Y.-M.C., D.J.S., Y.H., D.S.L.H., L.C., C.L., J.V., E.S.H., M.N., K.R.S., Q.T.O., N.P. and J.D.L. analysed and interpreted data. J.L., Y.-M.C., D.J.S., Y.H., D.S.L.H., L.C., J.R.B., C.A.P.B., M.N., J.B.R., K.R.S., M.B., Q.T.O., N.P., B.W.K., N.S. and J.D.L. wrote and reviewed the manuscript. K.R.S., M.B., Q.T.O., N.P., B.W.K., N.S. and J.D.L. provided administrative, technical or material support. J.D.L. supervised the study.

Competing interests N.S. is a co-inventor on a Cleveland Clinic patent on HSD3B1, and J.D.L. is listed as an inventor on Cleveland Clinic patents involving cancer therapeutics, both of which are not directly relevant to this manuscript. The other authors declare no competing interests.

Additional information

Supplementary information The online version contains supplementary material available at https://doi.org/10.1038/s41586-026-10451-5.

Correspondence and requests for materials should be addressed to Justin D. Lathia.

Peer review information *Nature* thanks Frederick Varn and the other, anonymous, reviewer(s) for their contribution to the peer review of this work. Peer reviewer reports are available.

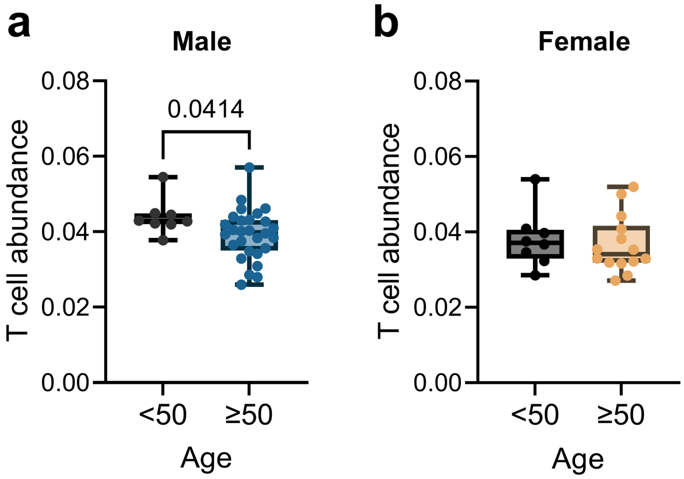

Extended Data Fig. 1 | Age dependent T cell abundance in male and female high-grade glioma (HGG). T cell abundance was measured after deconvoluting bulk RNA-seq on tumor samples obtained using image-guided biopsy. Average T cell value was obtained for each patient. **a**, Male HGG patients (n = 36 total), age <50 (n = 8), age ≥50 (n = 28). **b**, Female HGG patients (n = 22 total), age <50 (n = 8), age ≥50 (n = 14). Circles represent individual patients. Box plots show median, interquartile range and range. Statistics: Unpaired two-tailed Welch's t-test.

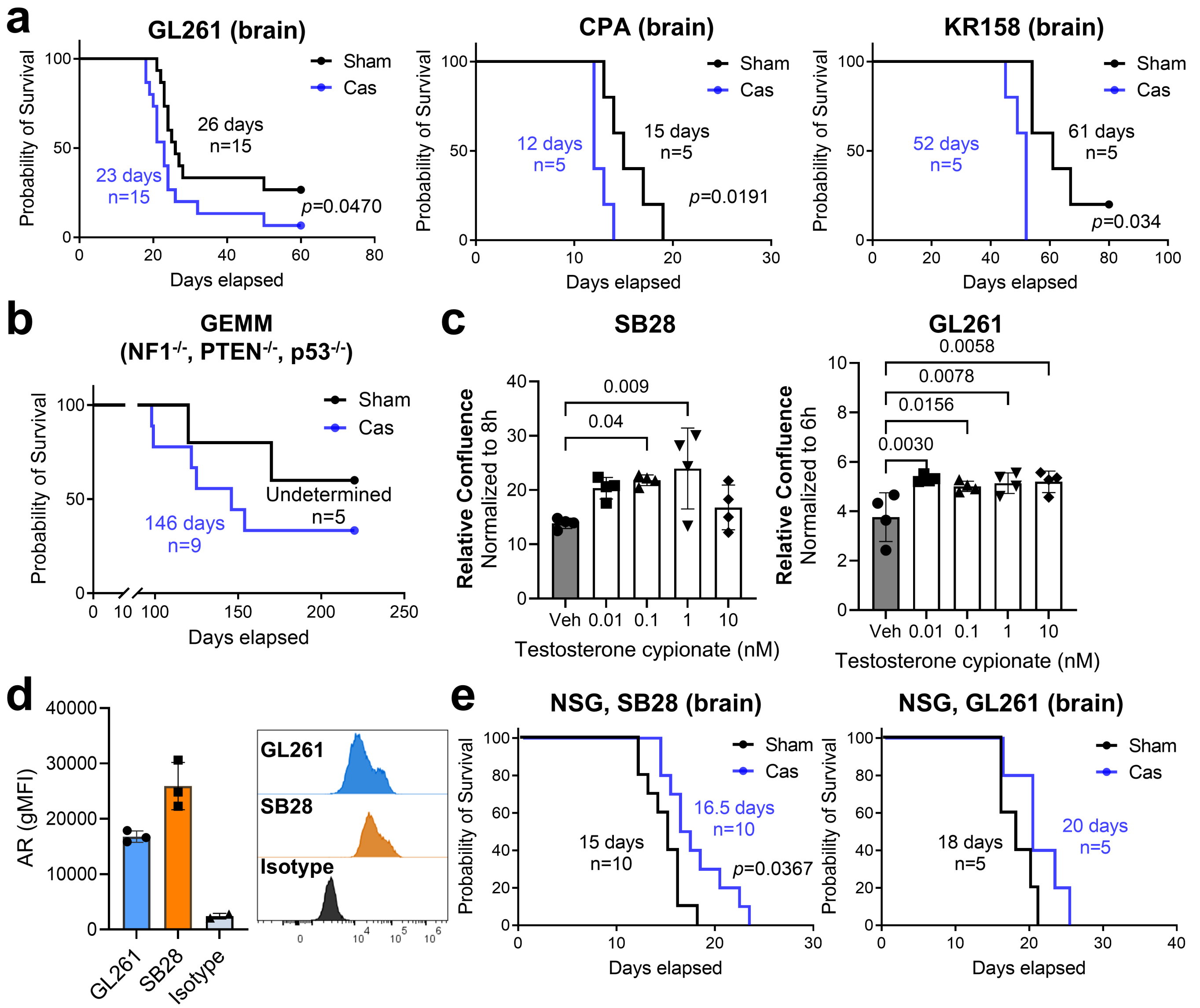

Extended Data Fig. 2 | Effects of androgens on GBM tumor growth in vivo and in vitro. a, Survival analysis of castrated or sham operated B6 mice after intracranial injection of murine syngeneic GBM cells. GL261 (25,000 cells), CPA (10,000 cells), KR158 (50,000 cells). Median survival days and the number of animals are indicated in the graph. **b**, Survival analysis of genetically engineered mouse model (GEMM) of GBM. **c**, SB28 or GL261 cells were cultured in the presence of various concentrations of testosterone cypionate or vehicle (corn oil) for 120 h and 96 h, respectively. Cell number was counted by Incucyte and normalized to 6 h. n = 4 biological replicates/group. **d**, Androgen receptor (AR) expression in murine GBM cells measured using flow cytometry. AR was stained after permeabilization. Data shown as mean±s.d. (left panel) and representative histogram (right panel). n = 3 biological replicates/group **e**, Survival analysis of NSG mice after intracranial implantation of SB28 cells (10,000 cells/mouse) or GL261 (20,000 cells/mouse). Median survival days and number of animals are indicated in the graph. Data are presented as mean ± s.d.; Statistics: Log-rank (Mantel-Cox) test (**a**,**b**,**e**), One-way ANOVA with Dunnett's multiple comparisons (**c**).

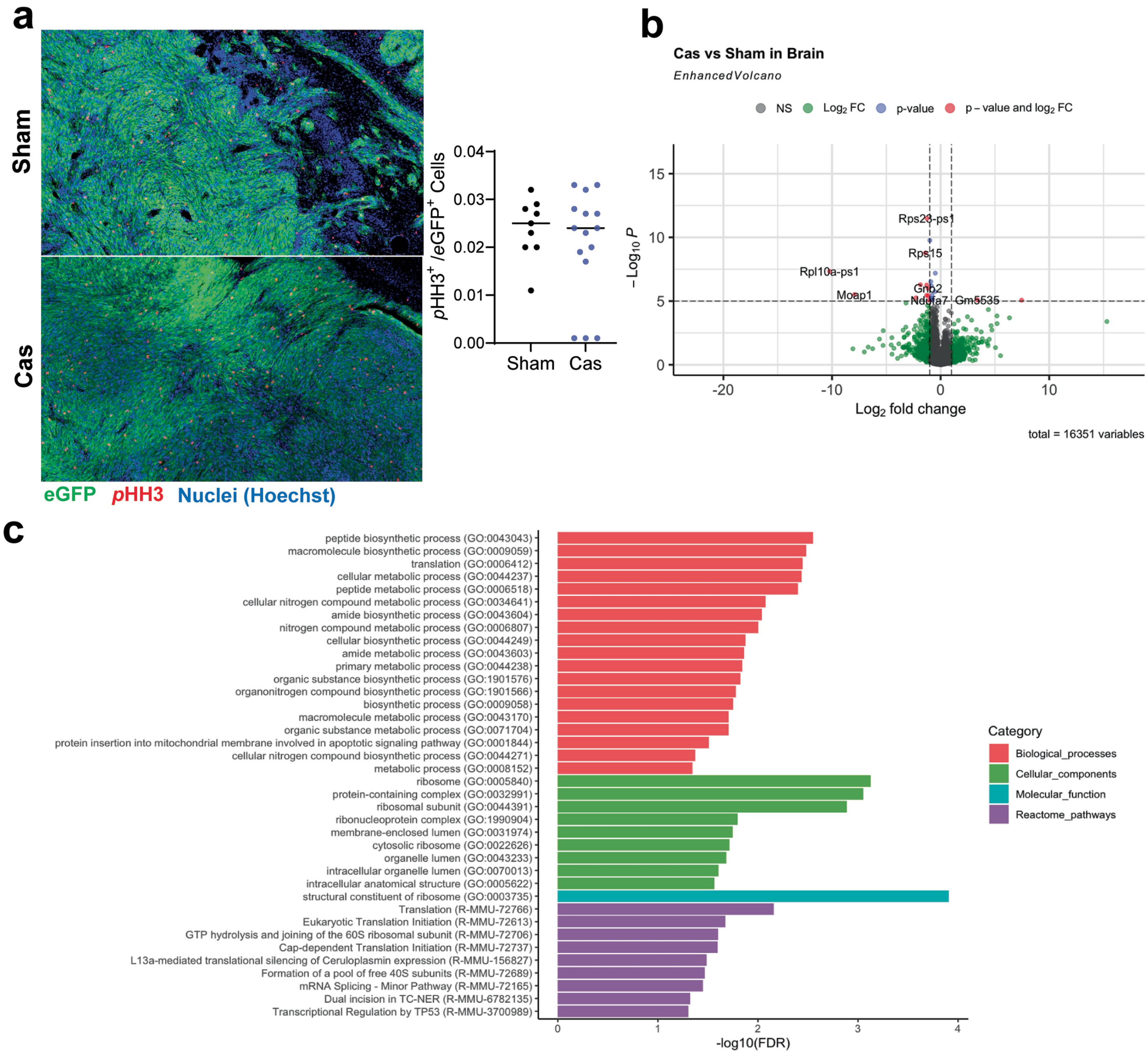

Extended Data Fig. 3 | No castration effect on tumor cell growth in vivo in an immune-competent brain tumor model. a, Immunofluorescence analysis of SB28 brain tumor bearing tissues from castrated or sham B6 mice. Mitotic tumor cells (eGFP; green) identified with phosphorylated histone H3 (pHH3; red), nuclei (Hoechst; blue). scale bar = 100 µm. *Left*: Representative images from castrated and sham control animals, *Right*: Quantification of phosphorylated histone H3+ cells normalized to nucleated, eGFP+ tumor cells. Median is indicated. n = 9/sham, n = 15/cas. *n* indicates the number of biologically independent animals. **b-c**, RNA-seq on tumor tissue collected from B6 mice on day 14 post intracranial implantation (SB28) following castration or sham surgery. **b**, Volcano plot showing differentially expressed genes between castrated and sham groups. Log2FC < −1 or > 1, p-value < 0.05. **c**, GO term enrichment analysis on downregulated DEGs in tumors from castrated mice compared to sham control. Statistics: Unpaired two-tailed t-test (**a**).

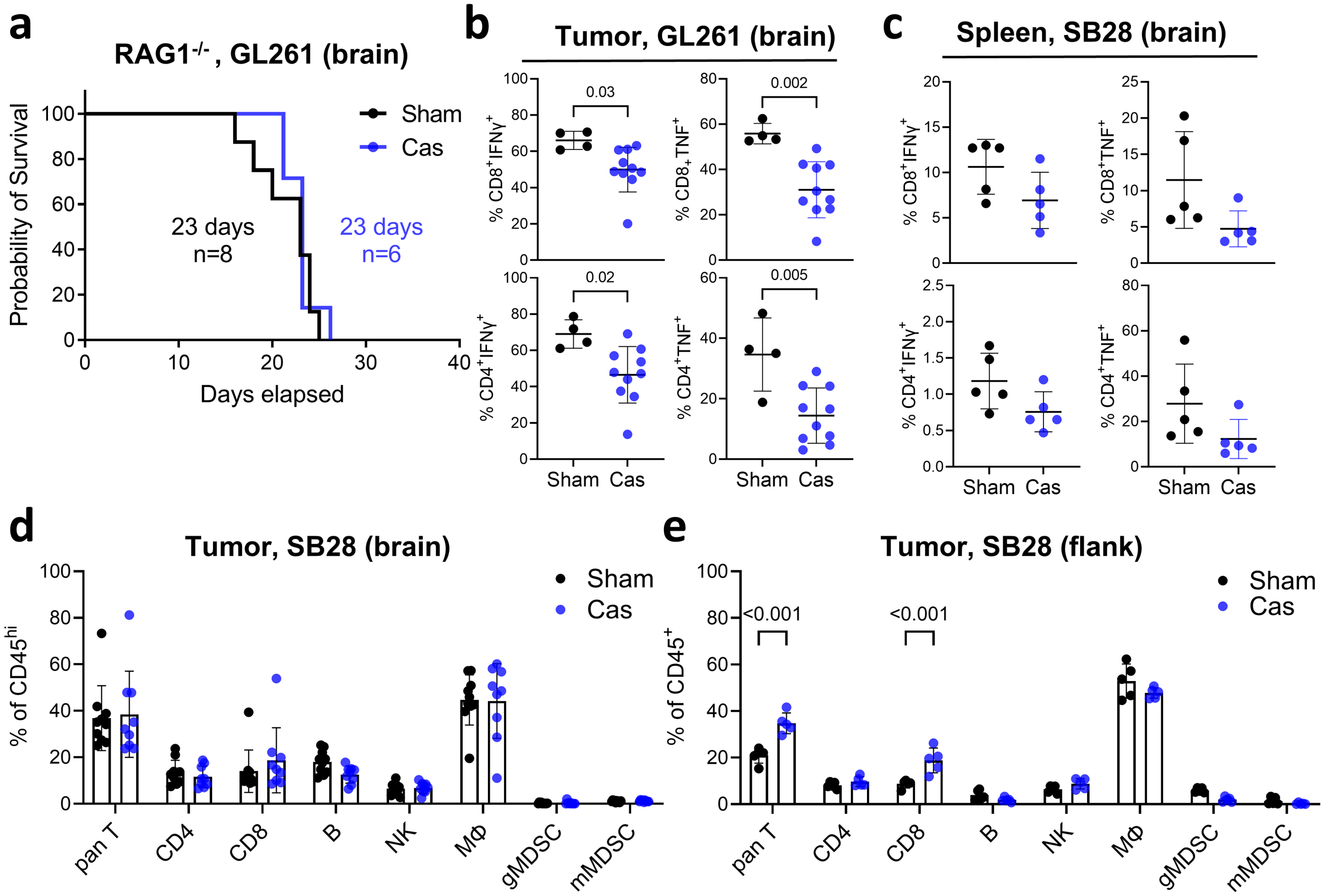

Extended Data Fig. 4 | Tumor location-dependent effect of castration on anti-tumor immunity. a, Survival of RAG1$^{-/-}$ mice after intracranial implantation of GL261 (25,000 cells/mouse) following sham or castration surgery. Median survival days and the number of animals are indicated in the graph. **b**, Intracellular expression of cytokines in T cells analyzed on day 17 from GL261 brain tumor (25,000 cells/mouse)-bearing mice. n = 4/sham, n = 10/cas. **c**, Intracellular expression of cytokines in T cells from spleen of mice bearing SB28 brain tumor. n = 5/sham, n = 5/cas. **d**, Frequency of immune cell subsets in the SB28 brain tumor measured on day 14 by flow cytometry. n = 10/sham, n = 9/cas. Data combined from two independent experiments. **e**, Frequency of immune cell subsets in the SB28 flank tumor measured on day 19 by flow cytometry. n = 5/sham, n = 5/cas. p = 0.000000007 (pan T), p = 0.0000128 (CD8). Data are presented as mean ± s.d.(**b**-**e**); Statistics: Log-rank (Mantel-Cox) test (**a**), Unpaired two-tailed t-test (**b,c**), Two-way ANOVA with Tukey's multiple comparison test (**d,e**).

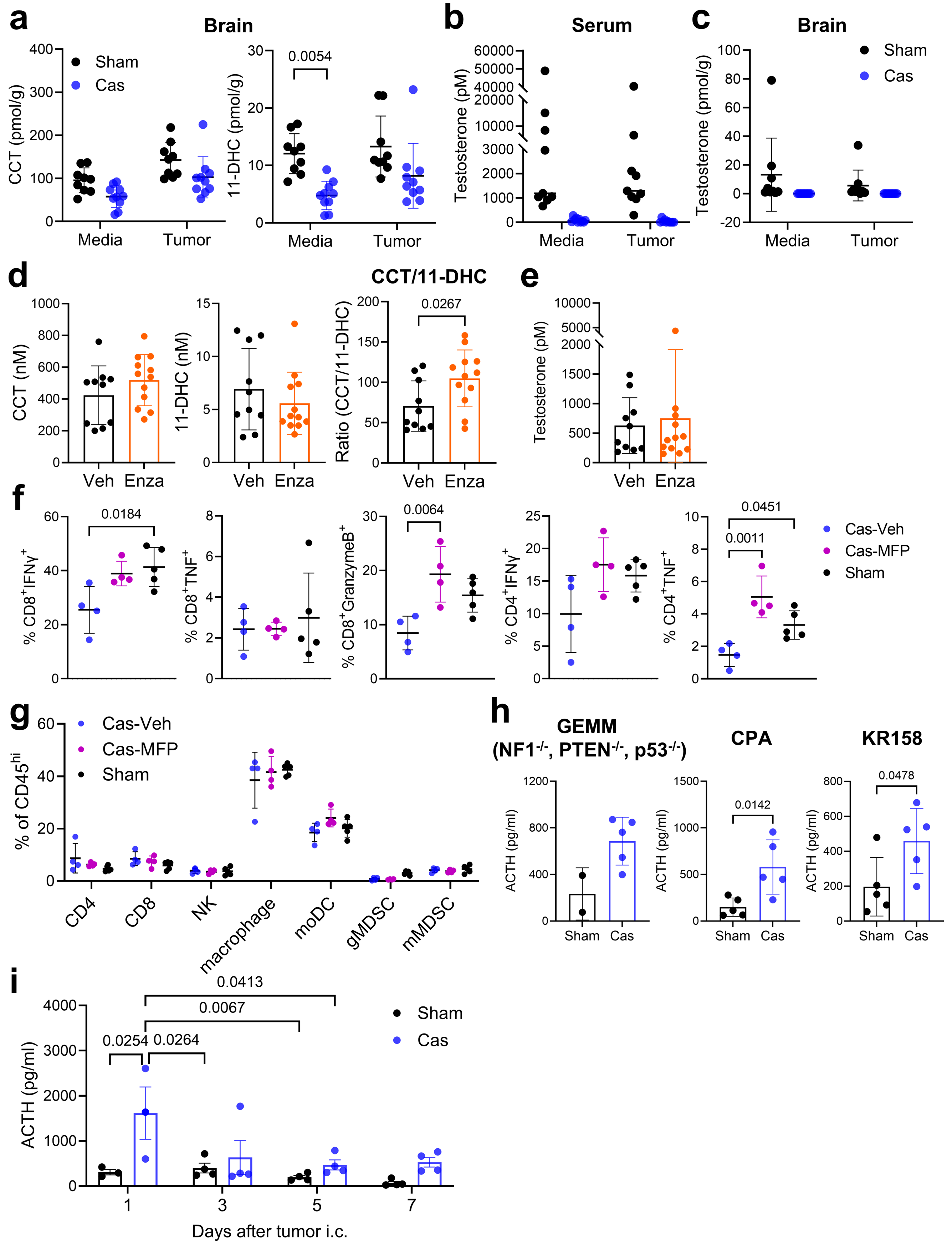

Extended Data Fig. 5 | See next page for caption.

Extended Data Fig. 5 | Alteration in steroid hormone levels and their effects on immune responses in brain tumor model following castration. **a-c**, Serum and brain samples were collected from castrated or sham-operated mice on day 14 post-intracranial implantation with SB28 (15,000 cells/mouse). n = 9/sham, n = 10/cas. **a**. Mass spectrometry analysis of corticosterone (CCT) and 11-dehydrocorticosterone (11-DHC) in brain tissue. **b-c**, Testosterone levels measured by mass spectrometry in serum (**b**) or brain tissue (**c**). **d-e**, Mass spectrometry analysis in serum collected at the endpoint from tumor-bearing mice (SB28; 15,000 cells/mouse) treated with vehicle (n = 10) or enzalutamide (n = 12). **d**, Serum levels of CCT, 11-DHC, and ratio of CCT/11-DHC. **e**, Serum testosterone levels. **f-g**, Castrated or sham-operated mice bearing brain tumors (SB28, 15,000 cells/mouse) were treated with mifepristone (MFP). Immune profiling was performed on day 14. n = 4/cas, n = 5/sham. **f**, Intracellular cytokine expression in T cells. **g**, Frequency of tumor infiltrating immune cell subsets. moDC: monocyte-derived dendritic cells. **h**, Serum ACTH levels measured at the endpoint. Data are derived from the same cohort used in Extended Data Fig. 2a,b. GEMM: n = 2/sham, n = 5/cas, CPA and KR158: n = 5/group. **i**, Serum ACTH levels measured at indicated time points after intracranial implantation of SB28 (15,000 cells/mouse). Day 1: n = 3/group, Day 3, 5, and 7: n = 4/group. Data are presented as mean ± s.d.; *n* indicates the number of biologically independent animals; Statistics: Two-way ANOVA with Tukey's multiple comparison test (**a-c,g,i**), Unpaired two-tailed t-test (**d,e,h**), One-way ANOVA with Tukey's multiple comparison test (**f**).

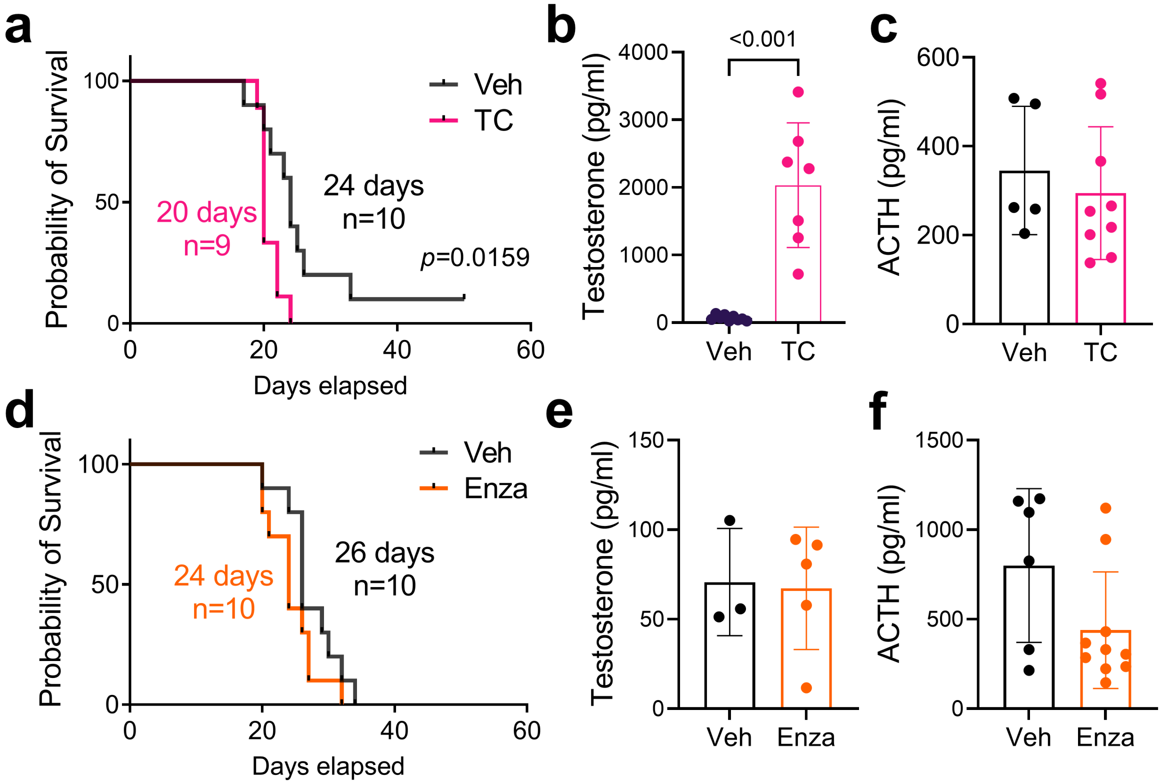

Extended Data Fig. 6 | Impact of androgen signaling on brain tumor progression in female mice. Six-week-old female C57BL/6 mice received intracranial implantation of SB28 cells (15,000 cells/mouse) and were treated with testosterone cypionate (TC, 12.5 mg/kg, s.c) (**a**-**c**) or enzalutamide (Enza, 10 mg/kg, i.p.) (**d**-**f**). **a**, Survival analysis of female B6 mice after testosterone cypionate treatment. Median survival days and the number of animals are indicated in the graph. **b**, Serum testosterone levels measured at the endpoint. n = 9/veh, n = 7/TC. **c**, Serum ACTH levels measured at the endpoint. n = 5/veh, n = 9/TC. **d**, Survival analysis of female B6 mice after enzalutamide treatment. Median survival days and the number of animals are indicated in the graph. **e**, Serum testosterone levels measured at the endpoint. n = 3/veh, n = 5/enza. **f**, Serum ACTH levels measured at the endpoint. n = 6/veh, n = 10/enza. Data are presented as mean ± s.d.; *n* indicates the number of biologically independent animals; Statistics: Log-rank (Manel-Cox) test (**a,d**), Unpaired two-tailed t-test (**b,c,e,f**).

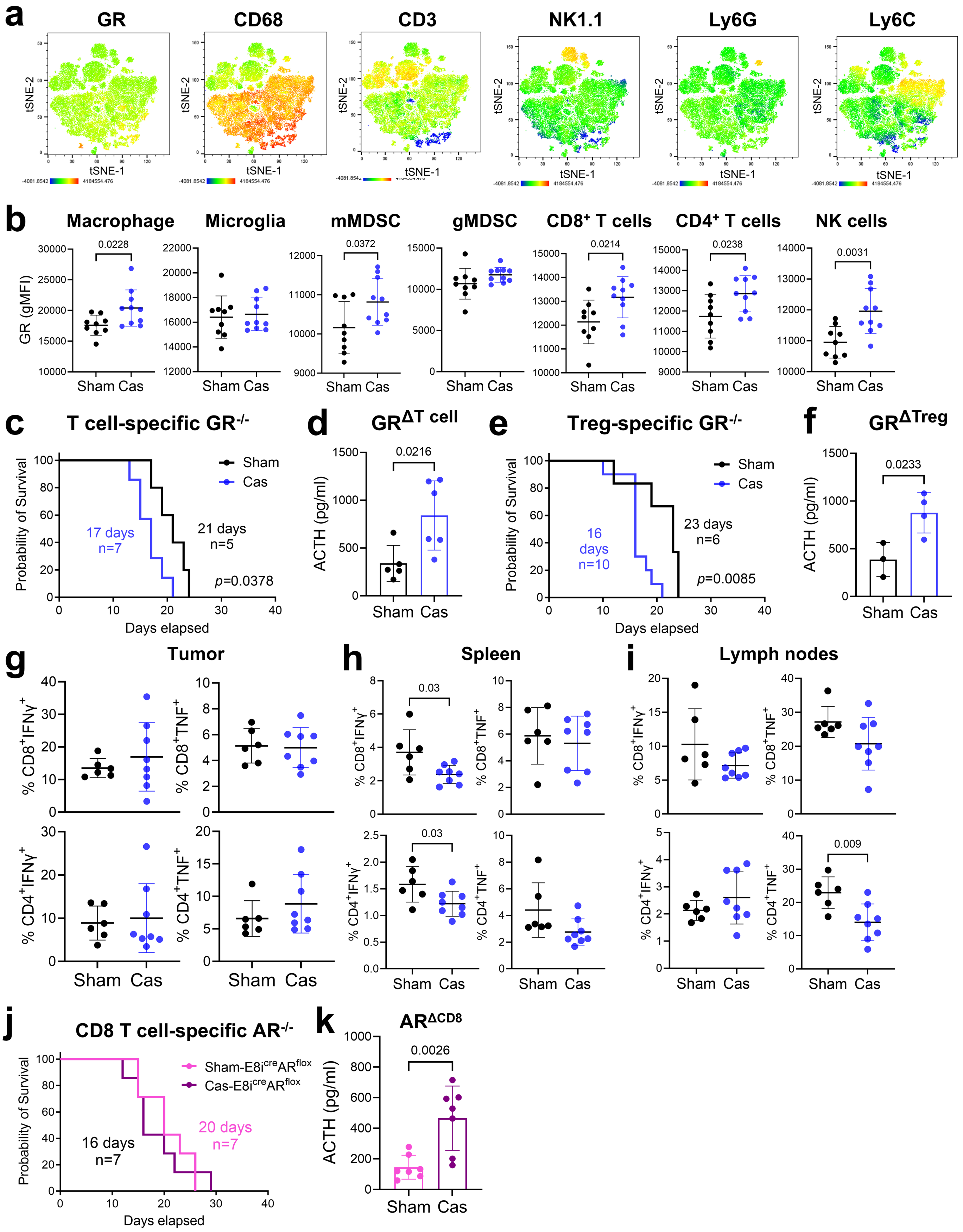

Extended Data Fig. 7 | See next page for caption.

Extended Data Fig. 7 | Increased glucocorticoids mediate immunomodulatory effect via myeloid cells in castrated mice. a-b, Flow cytometric analysis of tumor infiltrating immune cells from castrated or sham-operated mice 16 days after intracranial implantation of SB28 cells. n = 9/sham, n = 10/cas. **a**, t-SNE map displaying signal intensity of glucocorticoid receptor (GR) and immune cell markers. **b**, GR expression levels in each immune cell subset. **c**, Survival analysis of *Lck*^{cre}*Nr3c1*^{fl} mice after intracranial implantation of SB28 cells. Data combined from three independent experiments. **d**, Serum ACTH levels measured at the endpoint in *Lck*^{cre}*Nr3c1*^{fl} mice from (**c**). n = 5/sham, n = 6/cas. **e**, Survival analysis of *Foxp3*^{cre}*Nr3c1*^{fl} mice after intracranial implantation of SB28 cells. Data combined from four independent experiments. **f**, Serum ACTH levels measured at the endpoint in *Foxp3*^{cre}*Nr3c1*^{fl} mice from (**e**). n = 3/sham, n = 4/cas. **g-i**, *LysM*^{cre}*Nr3c1*^{fl} mice bearing brain tumor (SB28) were sacrificed on day 19. n = 6/sham, n = 8/cas. Intracellular cytokine expression in T cells from tumor (**g**), spleen (**h**) and lymph nodes (**i**). **j**, Survival analysis of castrated or sham operated *E8i*^{cre}Ar^{fl} mice intracranially implanted with SB28 tumors. **k,** Serum ACTH levels measured at the endpoint in *E8i*^{cre}Ar^{fl} mice from (**j**). n = 7/sham, n = 7/cas. Data are presented as mean ± s.d.; *n* indicates the number of biologically independent animals; Statistics: Unpaired two-tailed t-test (**b,d,f-i,k**), Log-rank (Manel-Cox) test (**c,e,g,j**).

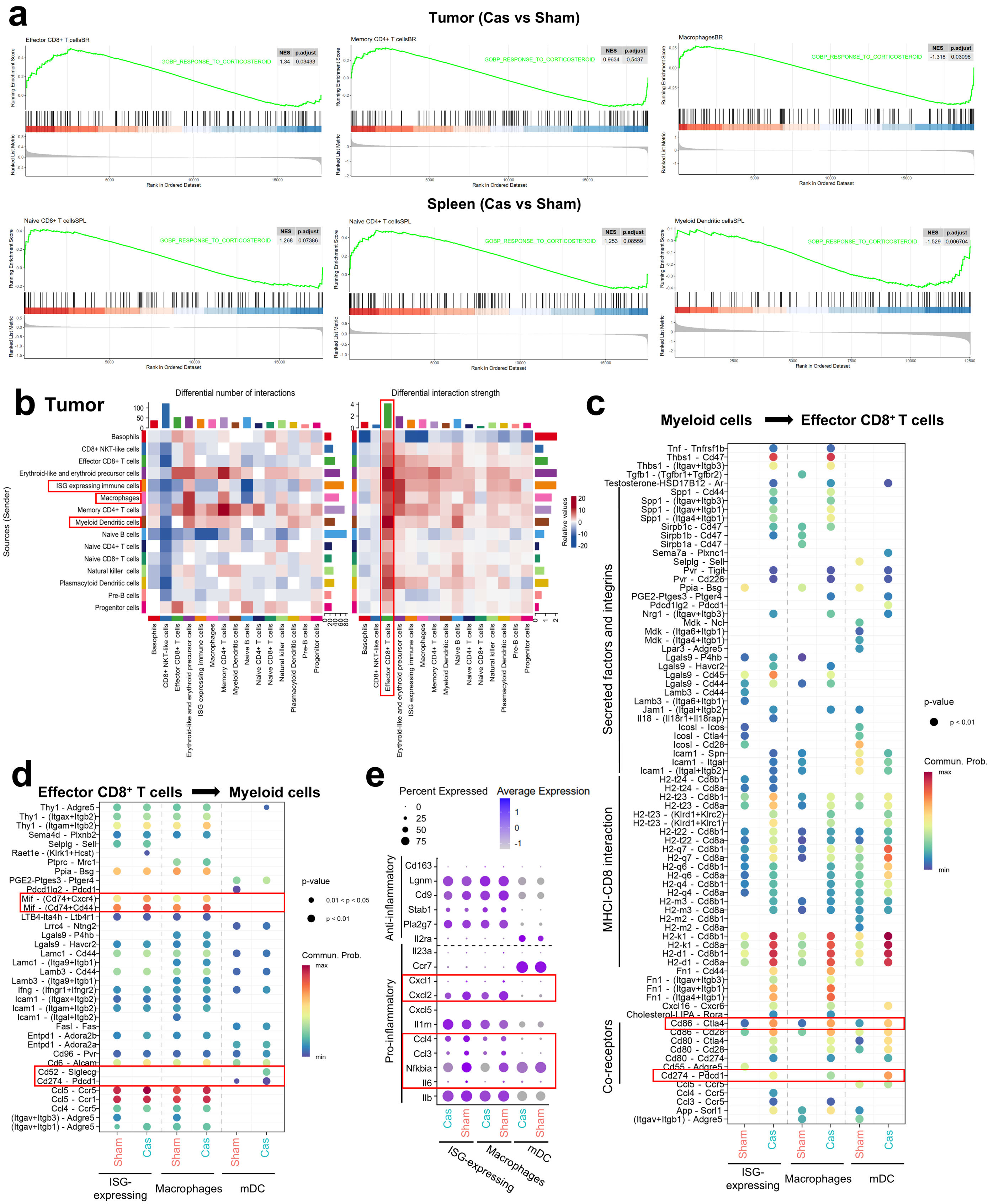

Extended Data Fig. 8 | See next page for caption.

Extended Data Fig. 8 | scRNA-seq revealed increased myeloid-T cell interaction in castrated mice. scRNA-seq was performed on CD45$^+$ immune cells isolated by FACS from tumor and spleen of brain tumor-bearing (SB28, day14) mice following sham or castration surgery. **a**, Gene set enrichment analysis (GSEA) of the immune cell subsets using the "Response to corticosteroid" gene set. **b-d**, Cell–cell communication analysis in tumor samples comparing castrated and sham mice using CellChat. **b**, Number and strength of interaction among immune cells in tumor. x-axis: receivers, y-axis: senders. **c-d**, Comparison of the significant ligand-receptor pairs between castrated and sham tumors, which contribute to the signaling between myeloid cells (IFN-expressing cells, macrophages, mDCs) and effector CD8$^+$ T cells. Dot color reflects communication probabilities and dot size represents significance of interactions (*p*-values). Empty space means the communication probability is zero. **e**, Pro- or anti-inflammatory gene expressions in each myeloid cell subset. Dot size represents the percentage of cells expressing the gene in the cluster. Dot color represents average expression level. Statistics: Permutation test (**a,c,d**).

a

Differentially expressed genes

Comparisons	Up	Down
Tumor: cas vs sham	47	6
Media: cas vs sham	8	5
Sham: tumor vs media	585	59
Cas: tumor vs media	466	7

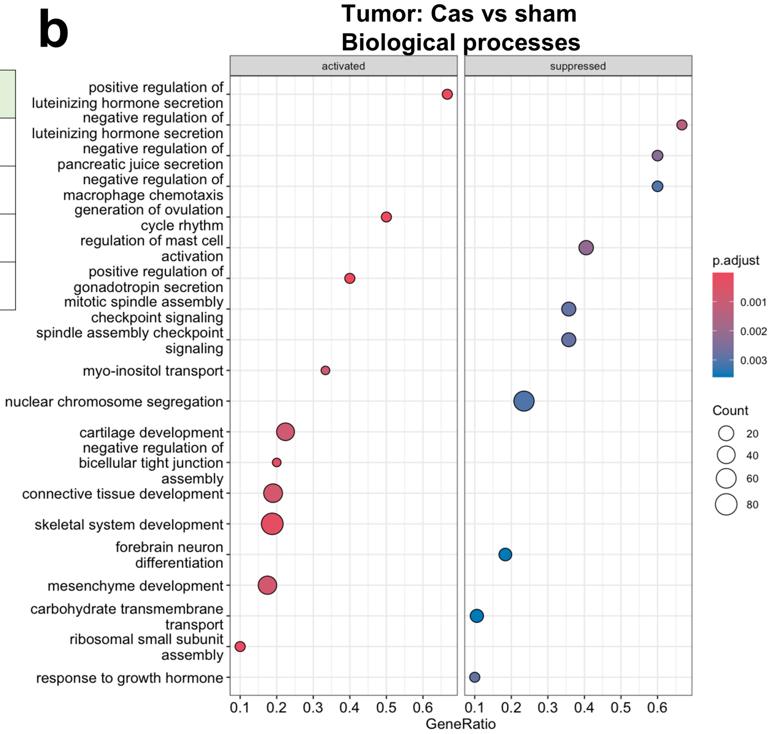

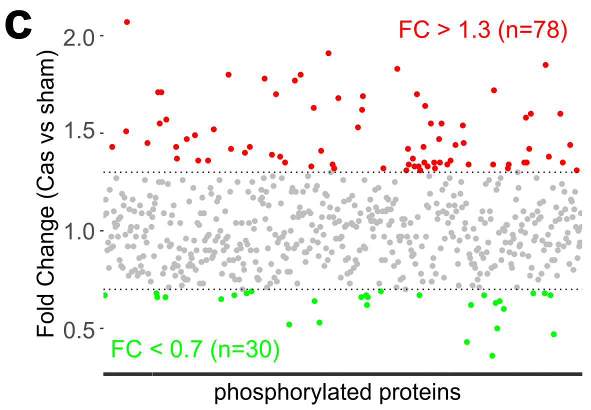

Extended Data Fig. 9 | RNAseq and phosphorylation array analysis of hypothalamus. a-b, Bulk RNAseq was performed on the hypothalamus tissue collected from castrated or sham-operated mice 14 days after intracranial implantation of SB28 cells (15,000 cells/mouse) or media. **a**, Differentially expressed genes (DEGs) identified in each comparison (cut-off: $Log_2FC > 1$ or < -1, adjusted p-value < 0.05). **b**, Gene Ontology term enrichment analysis of DEGs in tumor-bearing mice between castration and sham conditions. **c**, Phosphorylation array analysis of hypothalamus tissue from castrated or sham mice on day 14 post-intracranial injection of SB28 cells. The plot shows phosphorylated proteins with significant fold change (FC) between castration and sham conditions (FC > 1.3 or < 0.7). Statistics: Permutation test (**b**).

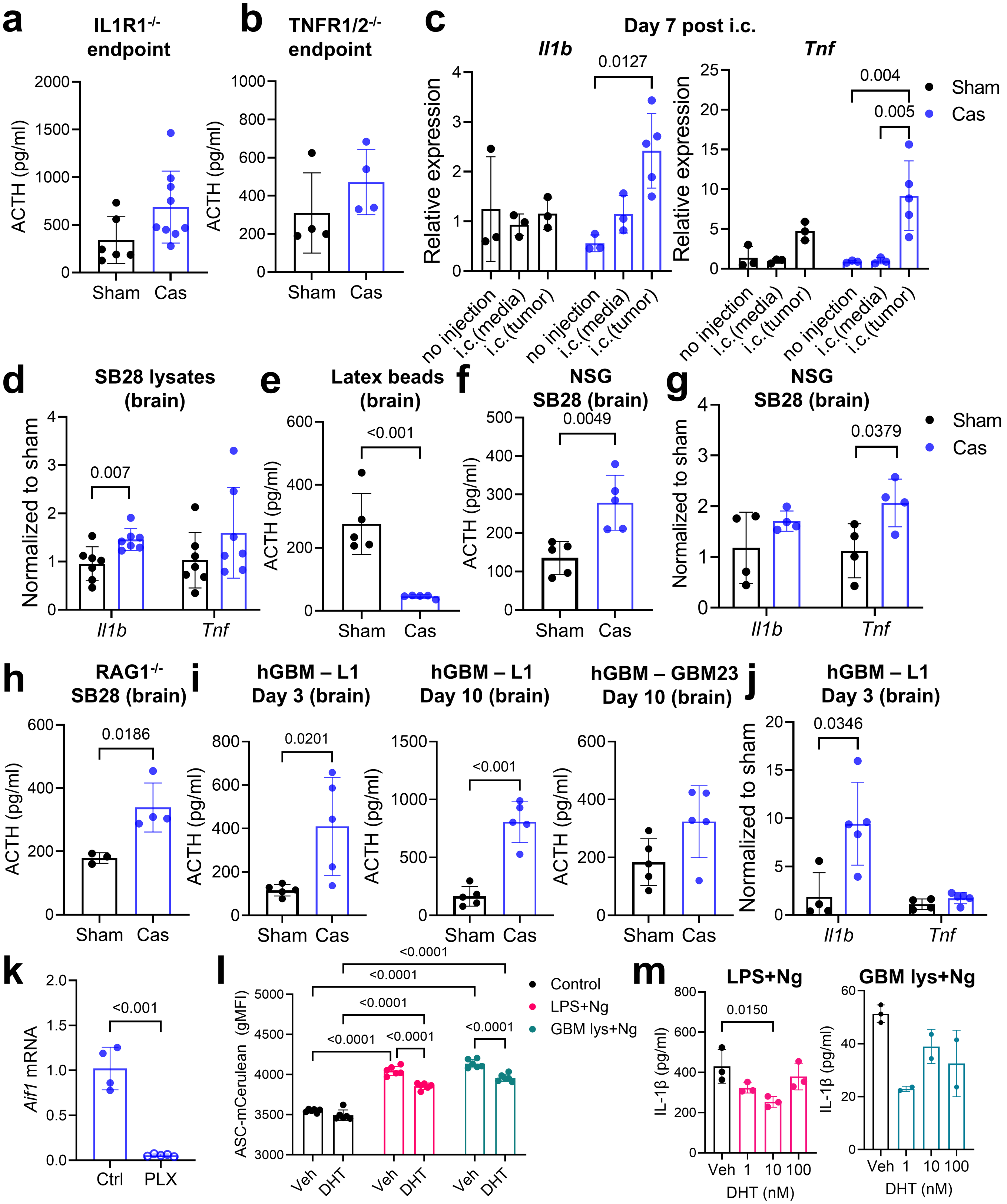

Extended Data Fig. 10 | See next page for caption.

Extended Data Fig. 10 | Increased proinflammatory cytokines in the brain of castrated mice with brain tumors. a-b, Serum ACTH levels measured at the endpoint in castrated or sham-operated IL1R1$^{-/-}$ (**a**) or TNFR1/2$^{-/-}$ (**b**) mice bearing SB28 brain tumors. IL1R1$^{-/-}$: n = 6/sham, n = 9/cas; TNFR1/2$^{-/-}$: n = 4/group. **c**, Tissue mRNA level measured in the brains of castrated or sham control mice 7 days after intracranial injection of media or tumor cells, or no injection. n = 3/group, except for n = 5/cas-i.c.(tumor). **d**, Tissue mRNA levels measured in the brains of castrated or sham control mice 3 days after intracranial injection with GBM lysates (SB28). n = 7/group. Data combined from two independent experiments **e**, ACTH level in serum samples collected on day 7 post-intracranial injection with latex beads. n = 5/group. **f-g**, Castrated or sham-operated NSG mice received intracranial injection of GBM cells (SB28) and sacrificed on day 7. **f**, Serum ACTH level. n = 5/group. **g**, Tissue mRNA levels. n = 4/group. **h**, ACTH level measured in serum samples from castrated or sham-operated RAG1$^{-/-}$ mice 7 days after intracranial implantation of SB28 cells. n = 3/sham, n = 4/cas. **i-j**, NSG mice were implanted with patient-derived human GBM cells (hGBM) following castration or sham surgery. **i**, Serum ACTH levels measured on day 3 or 10 post-implantation. n = 5/group. **j**, Tissue mRNA levels measured on day 3 post-implantation of L1 cells. n = 4/sham, n = 5/cas. **k**, Tissue mRNA level measured in the brains of castrated mice fed PLX3397-containing or control diet 7 days after intracranial injection of SB28 cells. n = 4/Ctrl, n = 5/PLX. $p = 0.000035$. **l-m**, Immortalized macrophages were cultured in the presence of dihydrotestosterone (DHT) or vehicle (methanol) for 72 h, followed by stimulation with LPS or murine GBM lysates and nigericin (Ng) for 4 h. **l**, ASC speck formation indicated by mCerulean signal intensity measured by flow cytometry. Representative data are shown from two independent experiments. **m**, Secreted IL-1β in supernatant was measured by ELISA. LPS+Ng: n = 3/group, GBM lys+Ng: n = 3/veh, n = 2/DHT group. Data are presented as mean ± s.d.; *n* indicates the number of biologically independent animals (**a-k**); Statistics: Unpaired two-tailed t-test (**a,b,e,f,h,k**), Two-way ANOVA analysis with Tukey's multiple comparison test (**c,l**), Multiple unpaired *t*-test (**d,g,j**), One-way ANOVA analysis with Sidak's multiple comparison test (**m**).

nature portfolio

Corresponding author(s): Justin D. Lathia

Last updated by author(s): Mar 13, 2026

Reporting Summary

Nature Portfolio wishes to improve the reproducibility of the work that we publish. This form provides structure for consistency and transparency in reporting. For further information on Nature Portfolio policies, see our Editorial Policies and the Editorial Policy Checklist.

Statistics

For all statistical analyses, confirm that the following items are present in the figure legend, table legend, main text, or Methods section.

n/a	Confirmed	
☐	☒	The exact sample size (*n*) for each experimental group/condition, given as a discrete number and unit of measurement
☐	☒	A statement on whether measurements were taken from distinct samples or whether the same sample was measured repeatedly
☐	☒	The statistical test(s) used AND whether they are one- or two-sided *Only common tests should be described solely by name; describe more complex techniques in the Methods section.*
☒	☐	A description of all covariates tested
☐	☒	A description of any assumptions or corrections, such as tests of normality and adjustment for multiple comparisons
☐	☒	A full description of the statistical parameters including central tendency (e.g. means) or other basic estimates (e.g. regression coefficient) AND variation (e.g. standard deviation) or associated estimates of uncertainty (e.g. confidence intervals)
☐	☒	For null hypothesis testing, the test statistic (e.g. *F*, *t*, *r*) with confidence intervals, effect sizes, degrees of freedom and *P* value noted *Give P values as exact values whenever suitable.*
☒	☐	For Bayesian analysis, information on the choice of priors and Markov chain Monte Carlo settings
☒	☐	For hierarchical and complex designs, identification of the appropriate level for tests and full reporting of outcomes
☒	☐	Estimates of effect sizes (e.g. Cohen's *d*, Pearson's *r*), indicating how they were calculated

Our web collection on statistics for biologists contains articles on many of the points above.

Software and code

Policy information about availability of computer code

Data collection	SpectroFlo v.3.3.0 (Cytek), FACSDiva v.9.-0 (BD Biosciences) were used for flow cytometry data collection. Incucyte Live-cell-Analysis system v2023a (Sartorius) was used to track cell count. Victor Nivo v.4.5.0 (Perkin Elmer) was used for reading ELISA plates. QTrap 5500 mass spectrometer (AB Sciex) was used for mass spectometry analysis. QuantStudio 5 (Applied Biosystems) was used for real-time PCR analysis. PhenoImager HT (Akoya Biosciences) was used for Image analysis. RNA-seq libraries were sequenced on Illumina NovaSeq 6000 (bulk and scRNA-seq) and NovaSeq X Plus (Spatial transcriptomics).
Data analysis	FlowJo v.10 (BD biosciences), Incucyte software v2020C (Sartorius), MultiQuant v.3.0.3 (AB Sciex), CIBERSORTx, GraphPad Prism v9 (GraphPad Prism Software), MultiQuant v.3.0.3. (AB Sciex), QuPath v.0.6.0. (QuPath), Ingenuity Pathway Analysis (Qiagen), Imaria v.10.2 (Imaris).

For manuscripts utilizing custom algorithms or software that are central to the research but not yet described in published literature, software must be made available to editors and reviewers. We strongly encourage code deposition in a community repository (e.g. GitHub). See the Nature Portfolio guidelines for submitting code & software for further information.

Data

Policy information about availability of data

All manuscripts must include a data availability statement. This statement should provide the following information, where applicable:

- Accession codes, unique identifiers, or web links for publicly available datasets
- A description of any restrictions on data availability
- For clinical datasets or third party data, please ensure that the statement adheres to our policy

The bulk RNA-seq, scRNA-seq, and spatial transcriptomics data have been deposited with links to BioProject in the NCBI BioProject database: PRJNA1254286 (RNA-seq on tumor), PRJNA1254297 (RNA-seq on hypothalamus), PRJNA1254695 (scRNA-seq on immune cells), PRJNA1372687 (spatial transcriptomics). For image-localized biopsy data analysis, data is publicly available at https://www.synapse.org/#!Synapse:syn52256644. Mouse reads were aligned to the GRCm38 (mm10) mouse reference genome and human reads were aligned to the GRCh37 human reference genome. Analysis details are provided in the Methods. All data generated in this study are available upon request from the corresponding author, Dr. Justin D. Lathia (lathiaj@ccf.org).

Research involving human participants, their data, or biological material

Policy information about studies with human participants or human data. See also policy information about sex, gender (identity/presentation), and sexual orientation and race, ethnicity and racism.

Reporting on sex and gender	Extended Data Figure 1 shows analysis of previously published dataset including patients' biological sex (Hu, L.S., D'Angelo, F., Weiskittel, T.M. et al. Integrated molecular and multiparametric MRI mapping of high-grade glioma identifies regional biologic signatures. Nat Commun 14, 6066 (2023). https://doi.org/10.1038/s41467-023-41559-1).
Reporting on race, ethnicity, or other socially relevant groupings	In Supplemental information for SEER analysis (Figure 1h-i), demographics of male GBM patients are indicated (Table 3).
Population characteristics	n/a
Recruitment	n/a
Ethics oversight	n/a

Note that full information on the approval of the study protocol must also be provided in the manuscript.

Field-specific reporting

Please select the one below that is the best fit for your research. If you are not sure, read the appropriate sections before making your selection.

☒ Life sciences ☐ Behavioural & social sciences ☐ Ecological, evolutionary & environmental sciences

For a reference copy of the document with all sections, see nature.com/documents/nr-reporting-summary-flat.pdf

Life sciences study design

All studies must disclose on these points even when the disclosure is negative.

Sample size	Sample sizes were chosen in excess to show a significant effect based on pilot experiments used to determine mean and spread.
Data exclusions	Data were examined using Grubbs' test and outliers were excluded with the criterion of alpha = 0.05.
Replication	All experiments were replicated as indicated in the corresponding figure legends.
Randomization	Mice were randomized for castration surgery or treatment, and for tumor implantation. For the in vitro experiments, samples with identical pretreatment conditions were randomly assigned to treatment groups.
Blinding	Flow experiments were not blinded during data collection or analysis, as tracking each group is critical for data interpretation. In some survival analysis, experiment groups were blinded to the investigators. Mass spectrometry analysis was blinded during data collection as the samples were labeled as group 1 and group 2.

Reporting for specific materials, systems and methods

We require information from authors about some types of materials, experimental systems and methods used in many studies. Here, indicate whether each material, system or method listed is relevant to your study. If you are not sure if a list item applies to your research, read the appropriate section before selecting a response.

Materials & experimental systems

n/a	Involved in the study	
☐	☒	Antibodies
☐	☒	Eukaryotic cell lines
☒	☐	Palaeontology and archaeology
☐	☒	Animals and other organisms
☒	☐	Clinical data
☒	☐	Dual use research of concern
☒	☐	Plants

Methods

n/a	Involved in the study	
☒	☐	ChIP-seq
☐	☒	Flow cytometry
☒	☐	MRI-based neuroimaging

Antibodies

Antibodies used

Antibodies for immune cell subsets:
For flow cytometry analysis:
CD11b (M1/70), BD Biosciences (#563553), surface 1:250;
CD69 (H1.2F3), BD Biosciences (#741234), surface 1:250;
CD11c (HL3), BD Biosciences (#612796), surface 1:250;
CTLA4 (UC10-4B9), BioLegend (#106312), Intra 1:250;
Ly6G (1A8), BD Biosciences (#560603), surface 1:250;
PD1 (29F.1A12), BioLegend (#135241), surface 1:250;
TIM3 (RMT3-23), BioLegend (#119727), surface, 1:100;
CD45R/B220 (RA3-6B2), BioLegend (#103237), surface 1:250;
Ki67 (16A8), BioLegend (#652413), Intra 1:250
TIM3 (RMT3-23), BioLegend (#119727), Intra 1:100;
CD3 (145-2C11), BD Biosciences (#564379), surface 1:250;
I-A/I-E (M5/114.15.2), BioLegend (#107606), surface 1:250;
CD45 (30-F11), BioLegend (#103132), surface 1:250;
Foxp3 (FJK-16s), eBioscience (#2260608), Intra 1:250;
LAG3 (C9B7W), BioLegend (#125224), surface 1:250;
NK1.1 (PK136), BioLegend (#108716), surface 1:250;
CD4 (GK1.5), BioLegend (#100422), surface 1:250;
CD8 (52-6.7), BioLegend (#100712), surface 1:250;
CD206 (C068C2), BioLegend (#141712), Intra 1:250;
Ly6C (HK1.4), BioLegend (#128024), surface 1:250;
CD68 (FA-11), BioLegend (#137024), intra 1:250;
F4/80 (BM8), BioLegend (#123117), surface 1:250;
IFN-γ (XMG1.2), BioLegend (#505846), Intra 1:250;
TNFα (MP6-XT22), BioLegend (#506329), Intra 1:250;
Granzyme B (QA18A28), BioLegend (#396414), Intra 1:250;
GR (NR3CR1) (BuGR2), eBioscience (#53-6189-82), Intra, 1:250
TCF1 (C63D9), cell signaling (#6709), intra, 1:250

For histology analysis:
1) 1' antibodies - 1:1000 dilution
cleaved caspase-3 (Asp175), Cell Signaling (#9662)
GFP, Aves Labs (#GFP-1020)
phospho-Histone H3 (Ser10), Cell Signaling (#9701)
cFos, EnCor Biotechnology (#RPCA-c-FOS)
Iba-1, Abcam (#ab5076)
ASC (AL,177), Adipogen (#AG-25B-0006-C100)

2) 2' antibodies - 1:500 dilution
Donkey anti-rabbit Alexa Fluor 488, Invitrogen (#A-21206)
Donkey anti-chicken Alexa Fluor 488, Invitrogen (#A-78948)
Donkey anti-rabbit Alexa Fluor 555, Invitrogen (#A-31572)
Rabbit anti-goat Alexa Fluor 647, Invitrogen (#A-21446)

For immunoblotting:
caspase-1 (p20), Adipogen (#AG-20B-0042-C100), 1:1000
beta-actin (AC-15), Sigma (#A5441-100ul), 1:10,000
Goat anti-mouse IR-670 secondary antibody, LiCor Bio (#92668070), 1:10,000

Validation

All antibodies used in this study are commercially available and were validated for specificity and applications by the manufacturers.

Eukaryotic cell lines

Policy information about cell lines and Sex and Gender in Research

Cell line source(s)

Mouse syngeneic glioma cell line SB28: female-derived, obtained from Dr. Hideho Okada (UCSF)

Cell line source(s)	Mouse syngeneic glioma cell line GL261: unknown sex-derived, obtained from the Developmental Therapeutic Program (NCI) Mouse syngeneic glioma cell line CPA: male-derived, obtained from the Castro-Lowenstein laboratory (University of Michigan) Mouse syngeneic glioma cell line KR158: unknown sex-derived, obtained from Dr. Loic Deleyrolle (Mayo clinic) Mouse syngeneic bladder carcinoma cell line MB49: male-derived, purchased from Animal Tumor Core (Cleveland Clinic) Mouse syngeneic melanoma cell line B16-F10: male-derived, shared by Dr. Thaddeus Stappenbeck (Cleveland Clinic) soon after they purchased the cells from ATCC (#CRL-6475) Glioblastoma patient-derived xenograft cell line L1: female-derived, originally from the laboratory of Dr. Brent Reynolds (University of Florida) (originally from the laboratory of Dr. Angelo Vescovi) Glioblastoma patient-derived xenograft cell line GBM23: male-derived, originally from the laboratory of Dr. Erik Sulman (MD Anderson Cancer Center).
Authentication	B16-F10 cells and MB49 were authenticated by the source. GBM cell lines were not further authenticated.
Mycoplasma contamination	All cell lines in our laboratory are routinely checked for mycoplasma. All cell lines used were tested negative.
Commonly misidentified lines (See ICLAC register)	No commonly misidentified cell lines were used in this study.

Animals and other research organisms

Policy information about studies involving animals; ARRIVE guidelines recommended for reporting animal research, and Sex and Gender in Research

Laboratory animals	All animals were kept in a specific pathogen-free facility of the Biological Resource Unit (BRU) at Lerner Research Institute, Cleveland Clinic., with a 12-hour light-dark cycle. 5-10 weeks old mice were used for this study. All mouse strains used in the study are listed in Supplementary Table 8.
Wild animals	This study did not involve wild animals.
Reporting on sex	Since this study focuses on elucidating the role of androgens in brain tumors, male mice were mostly used. In some experiments, female mice were used (Extended Data Figure 6).
Field-collected samples	This study did not involve samples collected from the field.
Ethics oversight	All animal procedures were performed in accordance with the guidelines and protocols approved by the Institutional Animal Care and Use Committee (IACUC) at the Cleveland Clinic.

Note that full information on the approval of the study protocol must also be provided in the manuscript.

Plants

Seed stocks	n/a
Novel plant genotypes	n/a
Authentication	n/a

Flow Cytometry

Plots

Confirm that:

☒ The axis labels state the marker and fluorochrome used (e.g. CD4-FITC).

☒ The axis scales are clearly visible. Include numbers along axes only for bottom left plot of group (a 'group' is an analysis of identical markers).

☒ All plots are contour plots with outliers or pseudocolor plots.

☒ A numerical value for number of cells or percentage (with statistics) is provided.

Methodology

Sample preparation	At the indicated time, mice were euthanized as described above, and brain tumor, spleen, and lymph nodes (inguinal) were harvested. Brain tumor tissue was minced into small pieces with scalpels and subjected to enzymatic digestion in the

	presence of collagenase D (1 mg/ml; Roche) and DNase I (0.1 mg/ml; Roche) at 37°C. Digested tissue was filtered through a 70 µm cell strainer. To enrich for immune cells, gradient centrifugation was performed using 30% percoll solution (Sigma). Red blood cells (RBCs) were lysed using RBC lysis buffer (BioLegend). For spleen and lymph nodes, tissue was ground onto a 40 µm cell strainer, followed by RBC lysis. All single-cell suspension samples were filtered once more with a 40 µm cell strainer before staining for flow anlaysis. For cell staining, after live/dead staining with LIVEDEAD Blue (Thermo Fisher Scientific) on ice for 15 min, cells were washed and incubated with FcR blocker (Miltenyi Biotech) diluted in PBS/2% BSA on ice for 10 minutes. For surface staining, cells were incubated in an antibody mixture diluted in brilliant buffer (BD Biosciences) at 1:100 to 1:250 on ice for 30 minutes. After washing with PBS/2% BSA buffer, cells were fixed with Foxp3/Transcription factor fixation buffer (eBioscience) overnight. For intracellular staining, antibodies were diluted in Foxp3/Transcription factor permeabilization buffer at a ratio of 1:250, and cells were incubated at room temperature for 45 minutes. For intracellular cytokine detection, cells were stimulated using Cell Stimulation Cocktail plus protein transport inhibitor (eBioscience) in complete RPMI for 4 hours, followed by the cell staining procedures described above. Stained cells were acquired with an Aurora (Cytek Biosciences) and analyzed using FlowJo software (v10, BD Biosciences).
Instrument	Cytek Aurora, BDFortessa
Software	SpectroFlow, FACSDiva
Cell population abundance	N/A
Gating strategy	Gating strategy is provided in the supplementary information (supplementary figure 1). After clean-up process, T cells were defined as CD3+CD45+ and each T cell subset was further identified using CD4, Foxp3, and CD8. Cytokine expression was defined using negative control without re-stimulation.

☒ Tick this box to confirm that a figure exemplifying the gating strategy is provided in the Supplementary Information.